Facile synthesis and enhanced photocatalytic activity of a novel $FeVO_4/Bi_4O_5Br_2$ heterojunction photocatalyst through step-scheme charge transfer mechanism

Tawanwit Luangwanta[a], Auttaphon Chachvalvutikul[a], Sulawan Kaowphong[a,b,c,d,*]

[a] Department of Chemistry, Faculty of Science, Chiang Mai University, Chiang Mai 50200, Thailand

[b] Center of Excellence in Materials Science and Technology, Chiang Mai University, Chiang Mai 50200, Thailand

[c] Materials Science Research Center, Faculty of Science, Chiang Mai University, Chiang Mai 50200, Thailand

[d] Environmental Science Research Center (ESRC), Faculty of Science, Chiang Mai University, Chiang Mai 50200, Thailand

*Corresponding author (Sulawan Kaowphong)

E-mail : sulawank@gmail.com; sulawan.k@cmu.ac.th

Tel: +66 (0)53 943341

Abstract

Construction of a step-scheme (S-scheme) heterojunction photocatalyst is currently under investigation as it is known to facilitate a decrease in the e^-/h^+ recombination rate and preserves a strong redox ability. This research work has reported on the use of microwave irradiation combined with the wet impregnation synthesis of $FeVO_4/Bi_4O_5Br_2$ heterojunctions at different weight percentages (%wt) of $FeVO_4$ (0.5, 1, 3 and 5%wt). The visible-light-driven photocatalytic activities for the photoreduction of Cr(VI), and the decontamination of certain organic pollutants (bisphenol A; BPA, rhodamine B; RhB, and tetracycline hydrochloride; TC) were also investigated. Ethylene glycol that was used as a reaction medium in the microwave synthesis process played a key role in the formation control of a flower-like structure of bismuth-rich $Bi_4O_5Br_2$. Among the heterojunction photocatalysts, $FeVO_4/Bi_4O_5Br_2$ with 1%wt of $FeVO_4$ markedly maximized the photocatalytic activity. Specifically, 95% of Cr(VI) was reduced by a reduction rate that was 6.0 times higher than that of $Bi_4O_5Br_2$. Similarly, this photocatalyst was able to degrade 90%, 97%, and 88% of BPA, RhB, and TC at degradation rates that were 2.0, 1.2, and 1.6 times higher than $Bi_4O_5Br_2$, respectively. Trapping experiments indicated that $\bullet O_2^-$ and h^+ were the main active species responsible for the organic pollutant degradation, while •OH played a minor role in this process. These outcomes were confirmed with the use of the nitrotetrazolium blue transformation method and the terephthalic acid photoluminescence probing technique. Enhancement in the photo-activity of 1%wt-$FeVO_4/Bi_4O_5Br_2$ was attributed to the extended visible-light absorption range as well as the efficient generation, separation, and migration of photo-generated charge carriers through the S-scheme charge transfer mechanism which was supported by the results from the trapping experiments, XPS and UV-vis DRS analyses, Ag and PbO_2 photo-deposition experiments, and electrochemical studies, along with the consideration of the reduction potentials of reactive oxygen species.

Keywords: Step-scheme; $FeVO_4/Bi_4O_5Br_2$; Heterojunction; Cr(VI) photoreduction; Organic pollutants degradation

1. Introduction

Currently, environmental pollution has proportionally increased to an irreversible stage due to the acceleration of industrial development and overpopulation trends. Large amounts of wastewater contaminated with heavy metal ions and organic pollutants have caused a variety of environmental and health problems [1,2]. Hexavalent chromium (Cr(VI)) is known to be one of the most toxic heavy metal ions and is regarded as a human carcinogen [3–5]. Furthermore, dye/non-dye organic pollutants and antibiotics are also known to be greatly harmful to aquatic life and aquatic ecosystems [6–8]. To date, developing effective strategies for the removal of these pollutants from wastewater has become a priority. Semiconductor-based heterogeneous photocatalysis is a promising strategy that can be used to resolve environmental contamination through the utilization of solar energy. To fully utilize this energy source, it is imperative that researchers explore and develop photocatalysts for the effective harvesting of visible light, which is representative of the majority of solar energy [1,2,9].

BiOBr is one of the most interesting visible-light-driven photocatalysts due to its layered structure with $[Bi_2O_2]^{2+}$ slabs placed in between double slabs of bromine ions. This structure helps to establish a static internal electric field that is essential for accelerating the separation and transfer of charge carriers and thus improving photocatalytic activity [10]. Recently, the bismuth-rich $Bi_4O_5Br_2$ photocatalyst has demonstrated a remarkable visible-light photocatalytic performance due to its relatively narrower energy band gap, higher optical absorption ability, and more efficient photogenerated charge separation and migration capabilities when compared with the stoichiometric BiOBr photocatalyst [11]. Moreover, it has

displayed a more negative conduction band potential that is favourable for photoreduction reactions, while its potential to be utilized in the oxidative degradation of organic pollutants has also been highlighted [12–16]. However, in practice, $Bi_4O_5Br_2$ has exhibited unsatisfied quantum efficiency due to a rapid e^-/h^+ recombination rate [11,17]. To resolve this limitation, $Bi_4O_5Br_2$ can be coupled with other semiconductors that convey suitable matching conduction and valence band potentials to form a heterostructure. Thus, we have identified a promising approach for the improvement of charge separation and charge transfer efficiency, resulting in improved photocatalytic performance [18,19].

In this research study, $FeVO_4$ was chosen to be coupled with $Bi_4O_5Br_2$ to feasibly form the $FeVO_4/Bi_4O_5Br_2$ heterostructure by considering the band position compatibility of both materials. $FeVO_4$ is an interesting photocatalyst owing to its high photostability and its visible-light responsive properties with a narrow band gap (2.05 eV) [20,21]. It has been demonstrated that $FeVO_4$ composited with bismuth-based photocatalysts, such as $BiVO_4$ [22], Bi_2O_3 [23], $Bi_7O_9I_3$ [24], and BiOCl [25], exhibited an improved visible-light driven photocatalytic performance for pollutant degradation. Therefore, this work aims to fabricate $FeVO_4/Bi_4O_5Br_2$ nanocomposites and evaluate their photocatalytic activities in terms of the reduction of toxic Cr(VI) ions to less toxic Cr(III) ions, and the degradation of bisphenol A and rhodamine B (models of colourless and coloured organic pollutants, respectively) and tetracycline hydrochloride (model of antibiotic contaminant) under visible-light irradiation. Firstly, $Bi_4O_5Br_2$ and $FeVO_4$ were synthesized with use of the microwave irradiation method. Under the microwave process, interactions between the electromagnetic radiation and conductive substances, including polar solvents, provide fast volumetric heating in the reaction solution system which yield nanomaterials with a highly crystalline structure and uniform particle size and shape. Herein, ethylene glycol was selected as a solvent for the microwave synthesis process of the $Bi_4O_5Br_2$ material because it possesses a high dielectric loss tangent (tan δ =

1.350 at 2.45 GHz and 20°C), allowing for a high conversion efficiency of the electromagnetic radiation into heat [26]. These materials were then combined to form $FeVO_4/Bi_4O_5Br_2$ nanocomposites using the wet impregnation method. Physicochemical, optical, electrochemical, and photocatalytic properties of the fabricated samples were investigated. Subsequently, the band alignment of the $FeVO_4/Bi_4O_5Br_2$ heterojunction and the charge transfer mechanism were proposed.

2. Experimental procedure

2.1. Fabrication of $FeVO_4$, $Bi_4O_5Br_2$, and $FeVO_4/Bi_4O_5Br_2$ nanocomposites

$Bi(NO_3)_3 \cdot 5H_2O$ and KBr at a molar ratio of 1:1 were separately dissolved in ethylene glycol (20.0 mL) and then mixed together under magnetic stirring (30 min). Subsequently, the mixture was irradiated using 2.45 GHz microwave radiation operating at 600 W for 110 cycles. The microwave power was set to 30 seconds on and 90 seconds off for each cycle. Finally, the obtained product was filtered, washed several times with deionized water, and dried. Deionized water was also used as a solvent in a comparison of the process. The synthesis of $FeVO_4$, and $FeVO_4/Bi_4O_5Br_2$ nanocomposites was similar to that of our previous reports [24,25]. The $FeVO_4$ contents in the $FeVO_4/Bi_4O_5Br_2$ nanocomposites were 0.5%, 1%, 3% and 5% by weight, and denoted as x%wt-$FeVO_4/Bi_4O_5Br_2$ nanocomposites where x was equal to 0.5, 1, 3 and 5, respectively. For the proposes of comparison, the $FeVO_4/Bi_4O_5Br_2$ composite was also prepared with physical mixing.

2.2. Material characterizations and electrochemical studies

X-ray diffraction (XRD) spectra were recorded on an X-ray diffractometer (Rigaku SmartLab). The morphology and particle size of the powders were examined with the use of a transmission electron microscope (TEM, JEOL JEM-2010) and a field emission scanning

electron microscope (FESEM, JEOL JSM-6335F) with an attached energy dispersive X-ray spectroscope (EDS). Optical properties were studied by UV-vis diffuse reflectance spectroscopy (UV-vis DRS, UV-1800 Shimadzu), and photoluminescence spectroscopy (PL, AvaSpec-2048TEC-USB2 Avantes) with an excitation wavelength of 345 nm. Chemical state and elemental composition were determined by X-ray photoelectron spectroscopy (XPS, AXIS ultra DLD, Kratos Analytical Ltd.) using an Al K_{α} X-ray source at 1.4 keV radiation. The specific surface area and total pore volume of the samples were investigated by N_2 adsorption at -196 ˚C using a Quantachrome instrument and calculated by the Brunauer-Emmett-Teller (BET) and Barrett-Joyner-Halenda (BJH) methods, respectively. Prior the analysis, the samples were degassed at 120 ˚C for 3 h under vacuum. Electrochemical impedance spectroscopy (EIS) spectra, Mott-Schottky plots, and photocurrent density curves were recorded on an electrochemical analyser (Metrohm autolab potentiostat/galvanostat, PGSTAT128N) with a standard three-electrode system, in which Ag/AgCl (3.0 M KCl) was used as the reference electrode, Pt wire was used as the counter electrode, and a sample film on a fluorine-doped tin oxide (FTO)-coated glass served as the working electrode. The 0.5 M Na_2SO_4 solution (pH ~ 6) was employed as an electrolyte solution.

2.3. Photocatalytic experiments

Photocatalytic activity was evaluated through the reduction of Cr(VI) and the degradation of organic pollutants (bisphenol A; BPA, rhodamine B; RhB, and tetracycline hydrochloride; TC). Briefly, the photocatalyst (100 mg) was dispersed in 200.0 mL of an aqueous solution of $K_2Cr_2O_7$ (20 mgL^{-1}), BPA (10 mgL^{-1}), RhB (10 mgL^{-1}), and TC (20 mgL^{-1}). The suspension was magnetically stirred in the dark for 30 min to establish an adsorption-desorption equilibrium on the photocatalyst's surface and was then irradiated under a 50 W LED lamp. After every 30 min of the reaction process, the suspension (3 mL) was

sampled, centrifuged, and then the concentrations of the remaining solutions were determined by measuring the maximum absorption wavelength (λ_{max}) at 276 nm for BPA, 554 nm for RhB, and 356 nm for TC using a UV-vis spectrophotometer (UV-1800, Shimadzu). For the Cr(VI) photoreduction, the sampling solutions were treated with 1,5-diphenylcarbazide and H_2SO_4 to form a Cr(VI)–diphenylcarbazide complex, which exhibited a maximum absorption intensity at λ_{max} of 543 nm. As a control, the same experiment was run without adding any photocatalysts. The equations used to calculate photocatalytic efficiency, and apparent rate constant (k_{app}) for Cr(VI) reduction, and organic pollutant degradation are provided in the Supporting Information. Total organic carbon (TOC) concentration in the supernatant solution was measured using a TOC analyzer (Muti N/C 3100, Analytik Jena AG, Germany).

Silver (Ag) and lead oxide (PbO_2) photo-deposition experiments were carried out to further confirm the charge transfer pathway in the $FeVO_4/Bi_4O_5Br_2$ heterojunction. The Ag photo-deposition procedure is explained as follows. First, the photocatalyst (20 mg) was dispersed in a $AgNO_3$ solution (1 mmol L^{-1}, 100.0 ml) under visible light irradiation for 360 min. Then, the photocatalyst with photo-deposited Ag was collected. It was then washed several times with deionized water and dried. For the PbO_2 photo-deposition, the experimental procedure was conducted under the same experimental conditions, except that a $Pb(NO_3)_2$ solution (1 mmol L^{-1}, 100.0 ml) was used as an oxidizing source. Depositions of Ag nanoparticles, and PbO_2 nanoparticles on the surface of the $FeVO_4/Bi_4O_5Br_2$ heterojunction were then investigated by TEM.

3. Results and Discussion

3.1. Physicochemical, optical, and electrochemical properties of the photocatalysts

XRD spectra of the synthesized powders are shown in **Figure 1**. XRD patterns of $Bi_4O_5Br_2$ and $FeVO_4$ were indexed as monoclinic $Bi_4O_5Br_2$ (ICSD No. 94498) and triclinic

$FeVO_4$ (JCPDs No. 00-038-1372) structures, indicating that $Bi_4O_5Br_2$ and $FeVO_4$ were successfully synthesized by the microwave irradiation method. The broadening of the diffraction peaks implied that the crystallite sizes of the $Bi_4O_5Br_2$ and $FeVO_4$ particles were within the nanoscale. It should be noted that by using water as a solvent, BiOBr with a tetragonal structure (JCPDs No.01-078-0348) was achieved (**Figure S1**(a)). These results suggest that ethylene glycol played an important role in the microwave synthesis of bismuth-rich $Bi_4O_5Br_2$. When compared with the water solvent, ethylene glycol possesses a higher viscosity, lower thermal conductivity, and lower dielectric constant which can lead to a slower diffusion rate of the reaction, thereby controlling the whole chemical reaction rates [27]. Consequently, a local concentration of bromide ions near BiO^+ ions in the ethylene glycol system could be decreased leading to a lower bromide content in the $Bi_4O_5Br_2$ material [28]. The XRD patterns of all $FeVO_4/Bi_4O_5Br_2$ nanocomposites are similar to that of $Bi_4O_5Br_2$, but without any obvious peaks of $FeVO_4$ owing to a much lower relative content of $FeVO_4$ in the nanocomposites. No peak shifts were observed suggesting that the crystal structure of $Bi_4O_5Br_2$ did not change after the introduction of $FeVO_4$ via the wet impregnation method.

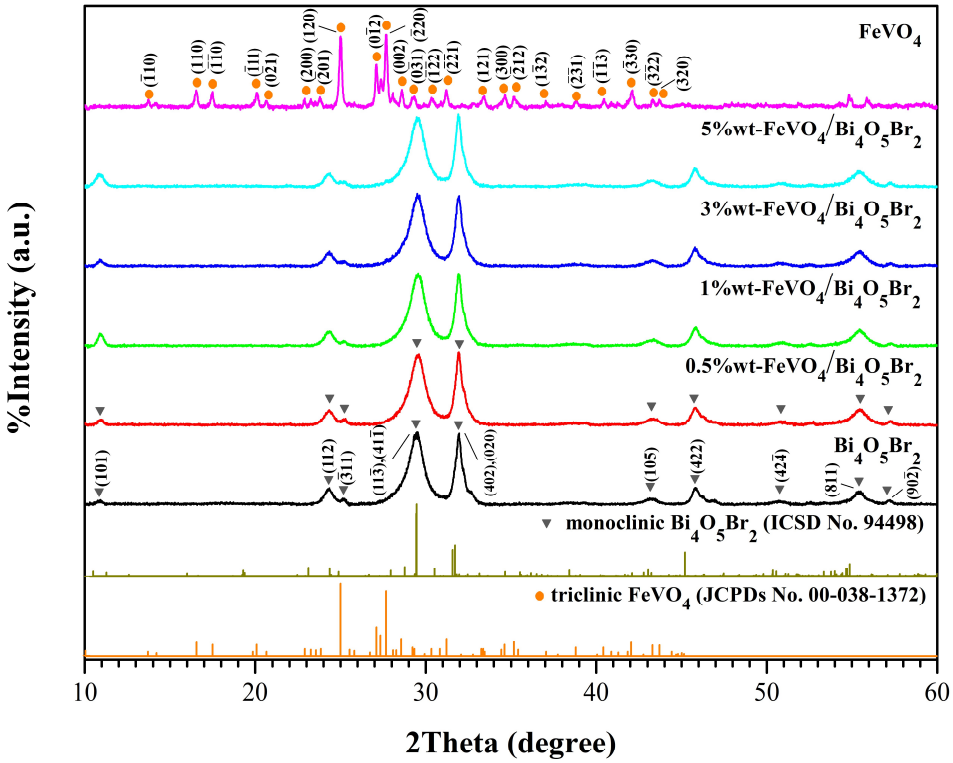

Figure 1. XRD patterns of the $Bi_4O_5Br_2$, $FeVO_4$, and $FeVO_4/Bi_4O_5Br_2$ nanocomposites with different contents of $FeVO_4$.

To further confirm the presence of $FeVO_4$ in the $FeVO_4/Bi_4O_5Br_2$ nanocomposites, the chemical states were analysed by XPS. **Figure 2**(a) shows that the XPS survey spectrum of $Bi_4O_5Br_2$ contained only the Bi, O, and Br elements, while the spectrum of $FeVO_4$ contained only the Fe, V, and O elements. For 1%wt-$FeVO_4/Bi_4O_5Br_2$, the signals of the Bi, O, Br, Fe, and V elements were observed. The C 1*s* peak at 286.4 eV was attributed to the adventitious carbon species in the XPS instrument. The high-resolution XPS spectra of Bi 4*f* in $Bi_4O_5Br_2$ (**Figure 2**(b)) exhibited two strong peaks at 159.2 and 164.5 eV, which corresponded to Bi $4f_{7/2}$ and Bi $4f_{5/2}$, respectively [29]. For 1%wt-$FeVO_4/Bi_4O_5Br_2$, the Bi $4f_{7/2}$ and Bi $4f_{5/2}$ signals shifted to 159.5 and 164.8 eV, respectively. These 4*f* signals indicated that the oxidation state of the Bi element was +3. **Figure 2**(c) shows the XPS spectra of O 1*s* in $Bi_4O_5Br_2$, $FeVO_4$, and

1%wt-$FeVO_4/Bi_4O_5Br_2$. For $Bi_4O_5Br_2$, the binding energy peaks located at 529.9 and 531.1 eV were ascribed to the Bi-O chemical bonds in the $[Bi_2O_2]^{2+}$ layers and the hydroxyl groups of the absorbed water molecules on the surface, respectively [15]. For $FeVO_4$, the peaks at 530.5 and 532.6 eV were attributed to the two chemical bonds of V−O and Fe−O, respectively [25]. For 1%wt- $FeVO_4/Bi_4O_5Br_2$, four sub-peaks located at 530.1, 531.3, 532.2, and 533.2 eV were observed. These sub-peaks could be ascribed to the Bi−O bonds in $Bi_4O_5Br_2$, O−H bonds in the surface-adsorbed water molecules, and V−O and Fe−O bonds in $FeVO_4$, respectively[25]. The XPS spectra of Br 3*d* in $Bi_4O_5Br_2$ (**Figure 2**(d)) can be divided into two peaks located at 68.4 and 69.4 eV, which corresponded to Br $3d_{5/2}$ and Br $3d_{3/2}$ of Br^- ion, respectively. The Br $3d_{5/2}$ and Br $3d_{3/2}$ signals of 1%wt-$FeVO_4/Bi_4O_5Br_2$ shifted to 68.6 and 69.6 eV. **Figure 2**(e) shows that the main XPS spectra of Fe $2p_{3/2}$ and Fe $2p_{1/2}$ of Fe^{3+} ion for 1%wt- $FeVO_4/Bi_4O_5Br_2$ (710.8 eV and 724.7 eV, respectively) appeared at lower energy than those of $FeVO_4$ (711.3 eV and 724.9 eV, respectively) [25]. The XPS spectra of V 2*p* in 1%wt-$FeVO_4/Bi_4O_5Br_2$ (**Figure 2**(f)) exhibited shifted peaks of V $2p_{3/2}$ (516.9 eV) and V $2p_{1/2}$ (524.4 eV) indicating the existence of V^{5+}. These signals appeared at lower energy than those in $FeVO_4$; V $2p_{3/2}$ (517.5 eV) and V $2p_{1/2}$ (525.1 eV). Generally, the binding energy is related to the change of electron density at the surface of the materials. The shifts in binding energy of the Bi 4*f*, Br 3*d*, Fe 2*p*, and V 2*p* for the $FeVO_4/Bi_4O_5Br_2$ heterostructure were ascribed to electron transfer at the interface between $FeVO_4$ and $Bi_4O_5Br_2$, which could be attributed to their different Fermi levels [30,31]. This benefited the formation of an internal electric field at the interface [32,33]. Moreover, the shifts in the binding energy also confirm that the $FeVO_4/Bi_4O_5Br_2$ nanocomposite has an interfacial chemical interaction between $FeVO_4$ and $Bi_4O_5Br_2$, which then facilitates the charge transfer process between the two components [34].

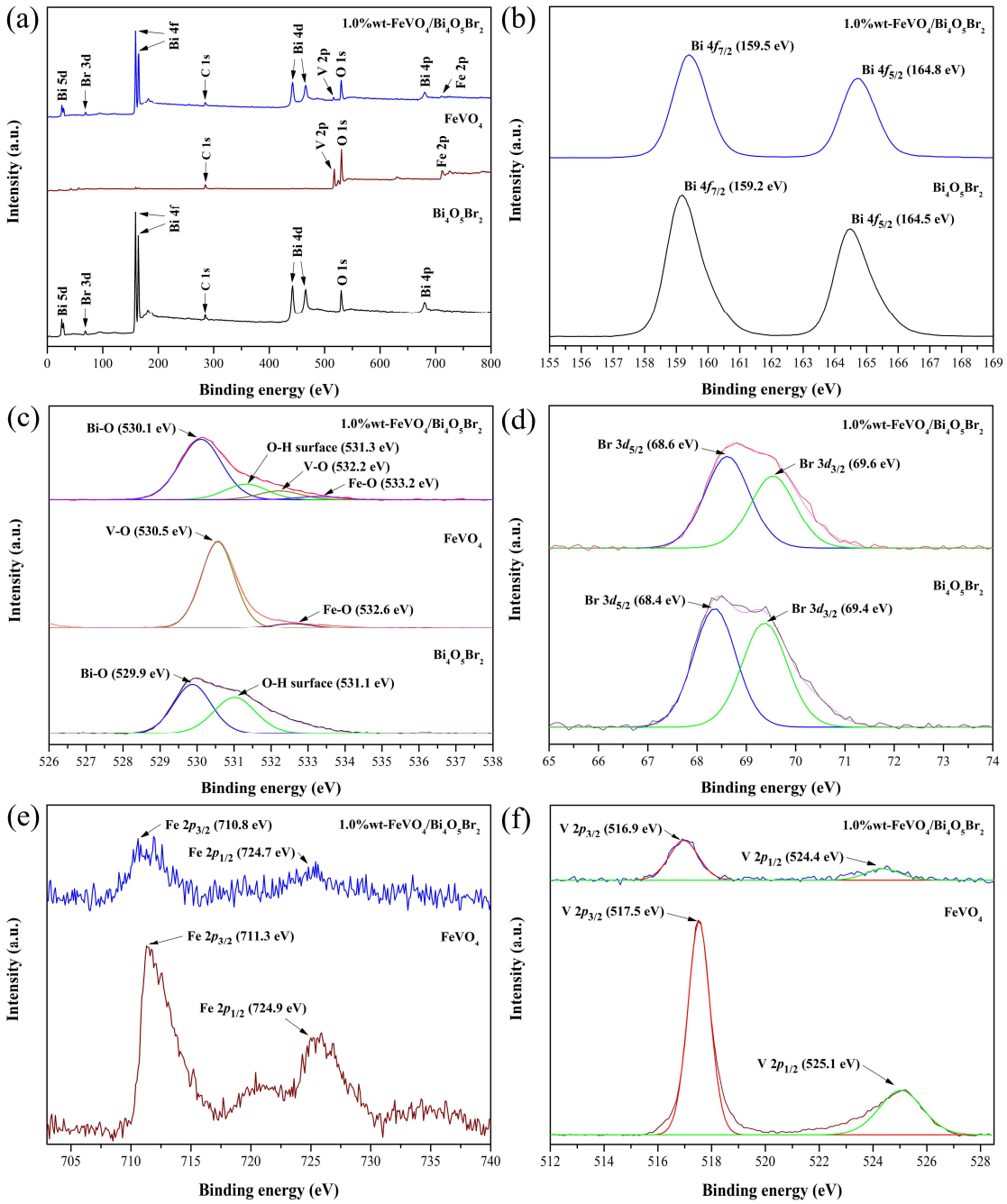

Figure 2. (a) XPS survey spectra and high-resolution spectra of (b) Bi 4*f*, (c) O 1*s* (d) Br 3*d* (e) Fe 2*p*, and (f) V 2*p* in 1%wt-$FeVO_4/Bi_4O_5Br_2$ in comparison with $Bi_4O_5Br_2$ and $FeVO_4$.

The FESEM image of the $Bi_4O_5Br_2$ powder synthesized using EG (**Figure 3**(a)) reveals a flower-like microsphere with a diameter of about 3.08 μm which is constructed of densely

packed nanosheets with a thickness of about 42 nm. In contrast, the BiOBr powder synthesized using water was composed of interconnecting thin nanosheets with a thickness of about 100 nm (**Figure S1**(b)). The difference in morphology could be attributed to the physicochemical properties of the solvents used. As is known, different solvents possess different properties that can influence the diffusion rate of ions in the reaction solution and then regulate crystal nucleation and crystal growth [27,35]. Lower viscosity, higher dielectric constant, and higher thermal conductivity of the water solvent could facilitate higher diffusion rates of the reaction ions, which could then lead to an anisotropic growth of the produced tiny nuclei according to the Ostwald ripening process. Finally, thick and large nanosheets were formed by a dissolution of small crystals. Using EG as solvent, the growth of the nuclei was attributed to the oriented attachment, Ostwald ripening, and self-assembly processes [27]. Firstly, EG molecules could coordinate with Bi^{3+} ions to from bismuth alkoxides, and gradually produce BiO^{+} ions due to the given microwave energy. Bromide ions then slowly reacted with the BiO^{+} ions in the EG system to form tiny bismuth-rich $Bi_4O_5Br_2$ nuclei [28]. After that, these tiny nuclei grew up and aggregated together to form nanosheets with thinner and smaller size due to a relative lower diffusion rate of the ions in EG. Finally, the flower-like $Bi_4O_5Br_2$ structure with interconnecting thin nanosheets was formed by the self-assembly process [36].

The $FeVO_4$ powder (**Figure 3**(b)) was composed of nanoparticles with an average size of 110-130 nm. The FESEM image of the 1%wt-$FeVO_4$/$Bi_4O_5Br_2$ nanocomposite (**Figure 3**(c)) shows that $FeVO_4$ nanoparticles attach to the surface of flower-like $Bi_4O_5Br_2$ microsphere, which corresponds to the TEM image (**Figure 3**(e-g)). The EDS spectrum of 1%wt-$FeVO_4$/$Bi_4O_5Br_2$ (**Figure 3**(d)) reveals signals of Bi, Br, Fe, V, and O elements with a Bi:Br atomic ratio of 1.68, confirming the coexisting of bismuth-rich $Bi_4O_5Br_2$ and $FeVO_4$ in the nanocomposite. Moreover, the homogenous distribution of these elements throughout the nanocomposite material shown in the FESEM-EDS mapping **(Figures S**2(a-d)) supports the

formation of the $FeVO_4/Bi_4O_5Br_2$ heterojunction with an intimate contact between $Bi_4O_5Br_2$ and $FeVO_4$ materials. This outcomes would favour the migration of photogenerated charges and thereby promote its photocatalytic activity. HRTEM images shown in **Figure 3**(h and i) reveal that two sets of lattice fringes with *d*-spacing values of 0.842 and 0.521 nm can be assigned to the (101) and (110) planes of monoclinic $Bi_4O_5Br_2$ and tetragonal $FeVO_4$, respectively.

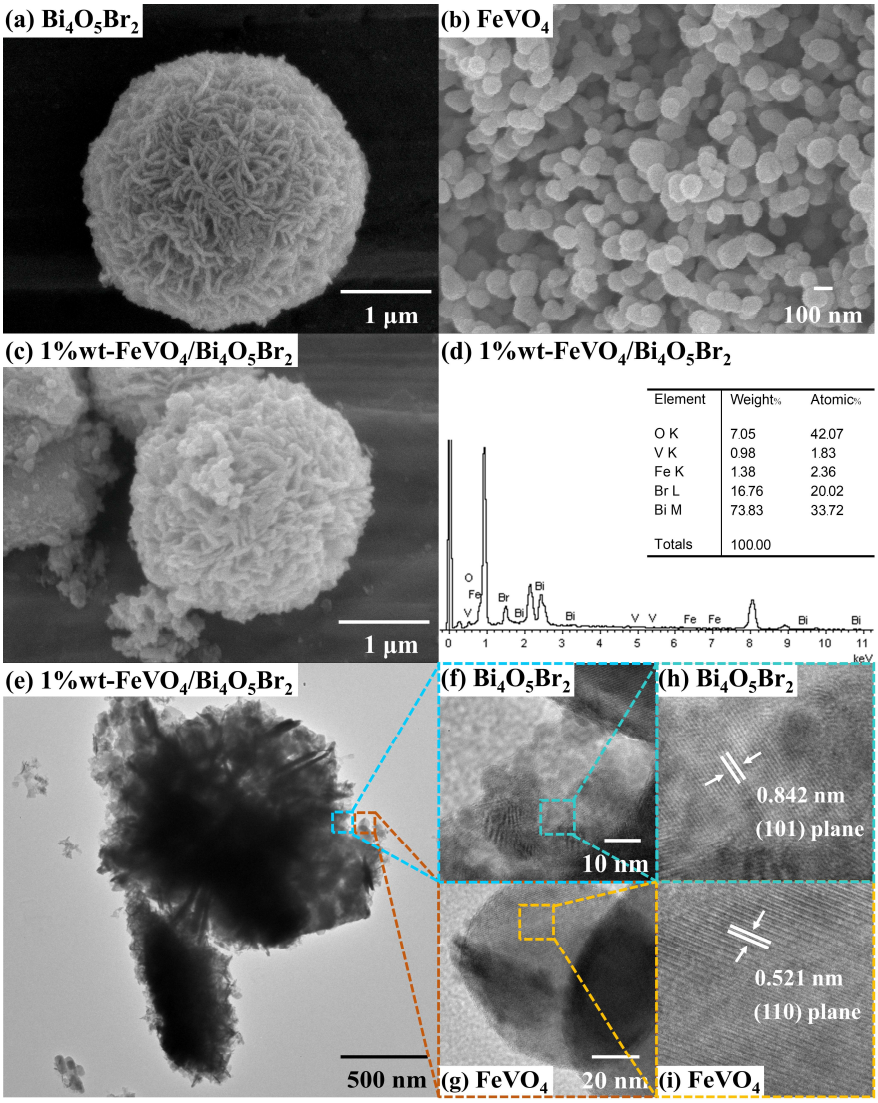

Figure 3. FESEM images of (a) $Bi_4O_5Br_2$, (b) $FeVO_4$ and (c) 1%wt-$FeVO_4/Bi_4O_5Br_2$. (d) EDS spectrum and (e) TEM image of 1%wt-$FeVO_4/Bi_4O_5Br_2$. HRTEM images of (f, h) $Bi_4O_5Br_2$ and (g, i) $FeVO_4$ in the nanocomposite.

UV-vis DRS spectra of $Bi_4O_5Br_2$ and $FeVO_4$ (**Figure 4**(a)) exhibited the onset of the absorption edges at 485 nm and 595 nm, respectively, indicating their visible-light absorption ability. With increasing $FeVO_4$ loading, the absorption edges of all $FeVO_4/Bi_4O_5Br_2$ nanocomposites were extended into a larger range of the visible-light region, and the light absorption ability increased when compared to $Bi_4O_5Br_2$. This suggests that the visible-light utilization of the nanocomposites was significantly improved. Band gap energy (E_g) was determined from the Tauc equation: $\alpha h\nu = A(h\nu - E_g)^{n/2}$ in which α, h, ν, E_g and A represent the absorption coefficient, Planck's constant, light frequency, band gap energy of the semiconductor, and the proportional constant, respectively. The n value equals to 1 and 4 for direct and indirect band gap materials, respectively. For both $Bi_4O_5Br_2$ and $FeVO_4$, n was equal to 4 [18,25]. From the plots of $(\alpha h\nu)^{1/2}$ versus hν (**Figure 4**(b)), the E_g values for $Bi_4O_5Br_2$ and $FeVO_4$ were 2.56 and 2.06 eV, respectively.

To determine the valence band and conduction band potentials of $Bi_4O_5Br_2$ and $FeVO_4$, the flat-band potentials (E_{FB}) of these two materials were evaluated using Mott-Schottky measurement at a frequency of 10 Hz. In **Figure 4**(c-d), the linear plots of the $Bi_4O_5Br_2$ and $FeVO_4$ electrodes show a positive slope, indicating that $Bi_4O_5Br_2$ and $FeVO_4$ are n-type semiconductors. By extrapolating the linear portion of the Mott-Schottky plots, E_{FB} of $Bi_4O_5Br_2$ and $FeVO_4$ were -0.05 and -0.53 V (*vs*. NHE), respectively. Generally, the conduction band potential (E_{CB}) of an n-type semiconductor is more negative by -0.1 V (*vs.* NHE) than the E_{FB} value [30]. Therefore, E_{CB} of $Bi_4O_5Br_2$ and $FeVO_4$ were -0.15 and -0.63 V (*vs.* NHE), respectively. Subsequently, the valence band potential (E_{VB}) of $Bi_4O_5Br_2$ and $FeVO_4$ were 2.41 and 1.43 V (*vs.* NHE), respectively.

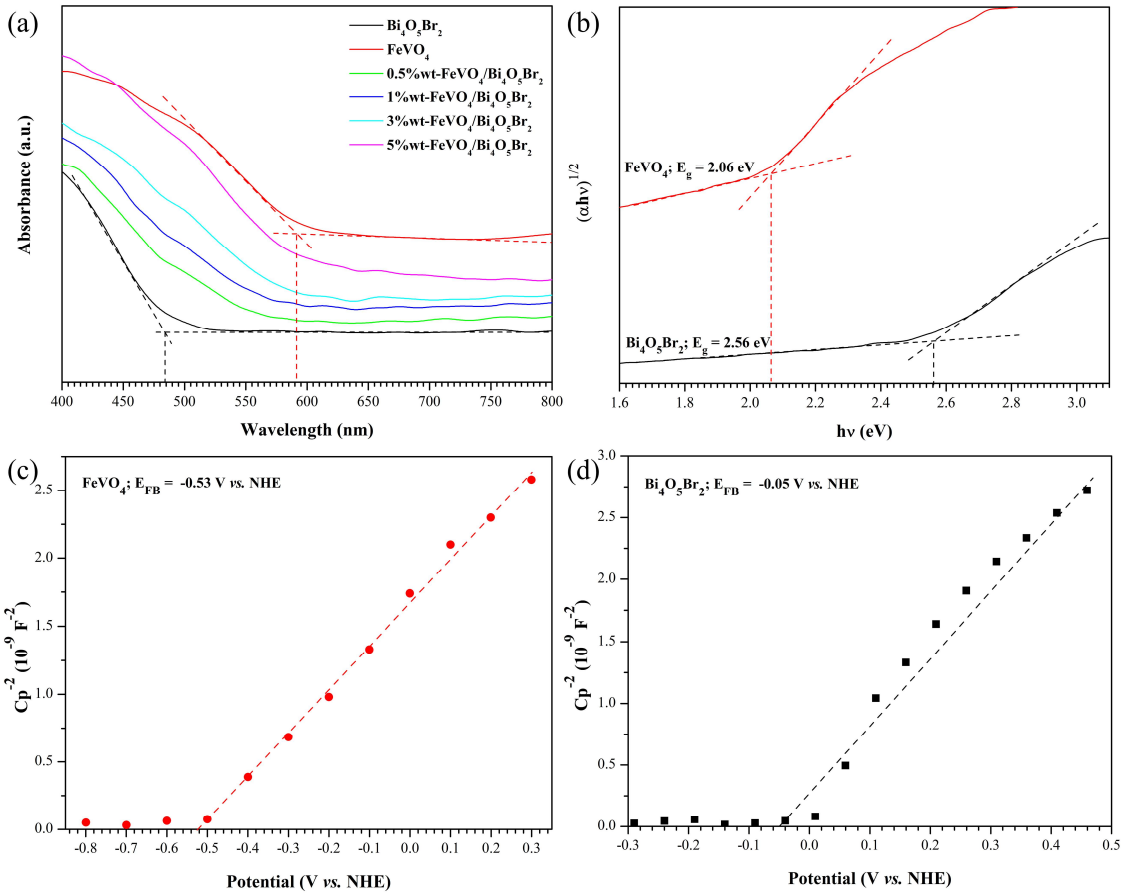

Figure 4. (a) UV-vis DRS spectra of $Bi_4O_5Br_2$, $FeVO_4$ and $FeVO_4/Bi_4O_5Br_2$. (b) Tauc plots of $Bi_4O_5Br_2$ and $FeVO_4$. Mott-Schottky plots of (c) $Bi_4O_5Br_2$ and (d) $FeVO_4$.

The EIS measurement was performed to verify the charge separation efficiency and charge transfer resistance of the $Bi_4O_5Br_2$, $FeVO_4$, and $FeVO_4/Bi_4O_5Br_2$ nanocomposites. Principally, the semicircle diameter of the Nyquist plot is proportional to the charge transfer resistance of the materials [37]. Among all electrodes, the Nyquist plot of the 1%wt-$FeVO_4/Bi_4O_5Br_2$ electrode (**Figure 5**(a)) exhibited the smallest semicircle diameter, reflecting the lowest charge transfer resistance. This finding implies an effective charge separation efficiency across the electrode/electrolyte interface and the fastest interfacial charge migration. Moreover, the lifetime of the photoinjected electrons (τ) of the photocatalysts could be determined via the following equation [38–40]; $\tau = 1/(2\pi f)$, where f represents the inverse

minimum frequency. **Figure 5**(b) shows the Bode-phase plots of the $Bi_4O_5Br_2$ and 1%wt-$FeVO_4/Bi_4O_5Br_2$ electrodes. The inverse minimum frequencies of $Bi_4O_5Br_2$ and 1%wt-$FeVO_4/Bi_4O_5Br_2$ were 15,489 and 10,000 Hz, respectively. Thus, based on this equation, the electron lifetime of 1%wt-$FeVO_4/Bi_4O_5Br_2$ (15.9 μs) was about 1.5 times longer than that of $Bi_4O_5Br_2$ (10.3 μs). The longer lifetime of the injected electrons of 1%wt- $FeVO_4/Bi_4O_5Br_2$ suggests the promoted interfacial charge transfer, which could effectively suppress the recombination rate of photogenerated e^-/h^+ pairs and promote charge separation in the $FeVO_4/Bi_4O_5Br_2$ heterojunction. Transient photocurrent responses of $Bi_4O_5Br_2$, $FeVO_4$ and 1%wt-$FeVO_4/Bi_4O_5Br_2$ (**Figure 5**(c)) show that 1%wt-$FeVO_4/Bi_4O_5Br_2$ exhibited a higher photocurrent density than the pristine materials suggesting that the construction of the $FeVO_4/Bi_4O_5Br_2$ heterojunction effectively improves the photogeneration of e^-/h^+ pairs as well as the charge separation efficiency under visible-light irradiation [41,42]. Moreover, the PL spectra of 1%wt-$FeVO_4/Bi_4O_5Br_2$ and $Bi_4O_5Br_2$ were recorded to evaluate the e^-/h^+ pairs recombination. Typically, a low PL emission intensity results from a low e^-/h^+ pairs recombination rate [43]. As is shown in **Figure 5**(d), the PL intensity of 1%wt-$FeVO_4/Bi_4O_5Br_2$ was lower than that of $Bi_4O_5Br_2$, indicating that combining $FeVO_4$ with $Bi_4O_5Br_2$ can suppress the e^--h^+ pair recombination. These results illustrate the improvements of separation and migration of the charge carriers as well as the decrease in the charge recombination in the 1%wt-$FeVO_4/Bi_4O_5Br_2$ heterojunction.

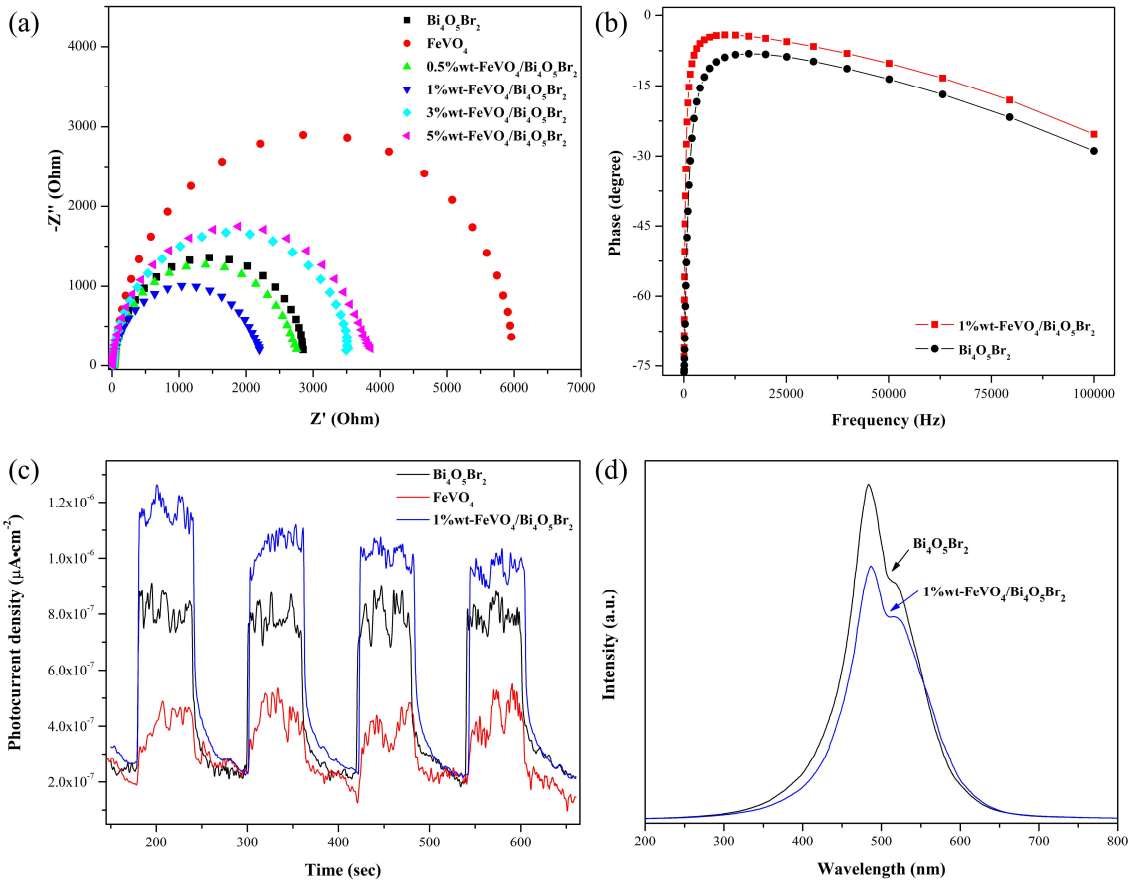

Figure 5. (a) EIS Nyquist plots, (b) Bode-phase plots, (c) transient photocurrent responses and (d) PL spectra of the materials.

3.2. Photocatalytic activity tests

3.2.1. Photocatalytic reduction of Cr(VI)

Photocatalytic activity of $Bi_4O_5Br_2$, $FeVO_4$, and $FeVO_4/Bi_4O_5Br_2$ for the Cr(VI) photoreduction at pH 5 (initial pH) under visible-light irradiation were investigated. Time-dependent absorption spectra of the Cr(VI)–diphenylcarbazide complex during the photoreduction by 1%wt-$FeVO_4/Bi_4O_2Br_5$ are depicted in **Figure S3**(a). The absorption bands of the Cr(VI)–diphenylcarbazide complex steadily decreased upon light irradiation and completely diminished within 120 min. There was no significant change in the Cr(VI) concentration in the absence of the photocatalyst, as is shown in **Figure 6**(a), demonstrating

that the self-photoreduction of Cr(VI) could be negligible. $Bi_4O_5Br_2$ and $FeVO_4$ reduced 51% and 15% of Cr(VI) with k_{app} of 6.5×10^{-3} and 8.0×10^{-4} min^{-1}, respectively. By combining 0.5 and 1%wt of $FeVO_4$ with $Bi_4O_5Br_2$, the photo-efficacies were increased to 56% and 95% with k_{app} of 1.3×10^{-2} and 3.9×10^{-2} min^{-1}, respectively. However, with further increases in $FeVO_4$ loadings (3 and 5 %wt), photo-efficacies were further decreased to 32% and 25% with k_{app} of 5.9×1^{-3} and 5.7×10^{-3} min^{-1}, respectively. Among the tested photocatalysts, 1%wt-$FeVO_4/Bi_4O_5Br_2$ provided the highest Cr(VI) photoreduction efficiency and the greatest reaction rate (**Figure 6**(b)).

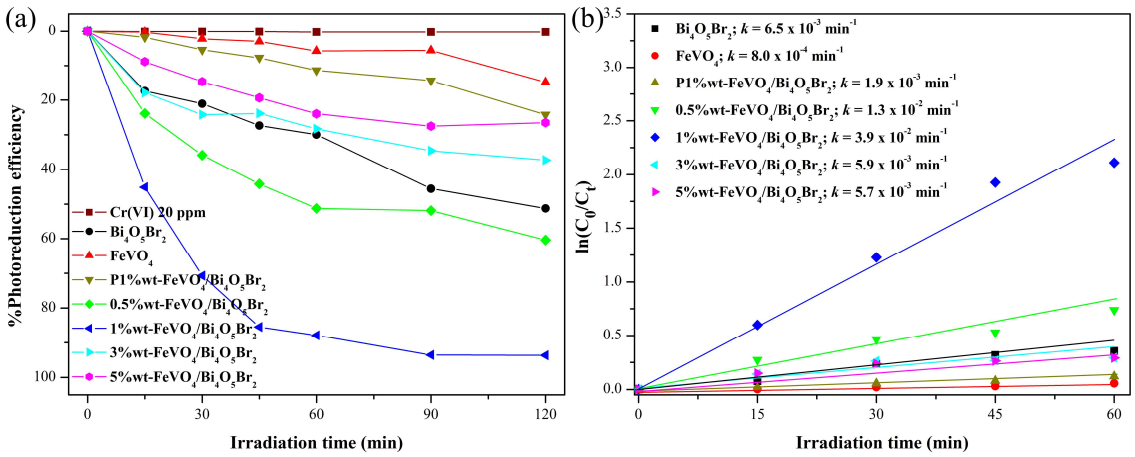

Figure 6. (a) %Photoreduction efficiency of Cr(VI) and (b) kinetic plots of $Bi_4O_5Br_2$, $FeVO_4$, and $FeVO_4/Bi_4O_5Br_2$ nanocomposite photocatalysts.

3.2.2. Photocatalytic degradation of organic pollutants

To further explore the practical applications of the constructed photocatalysts towards organic pollutant degradation, the degradation of BPA, RhB and TC was also studied. As is shown in **Figure 7**, the poor photodegradation of BPA and RhB in the absence of the photocatalysts indicated that the photolysis of these organic compounds could be neglected, while the slight degradation of TC was due to the susceptibility to white light [44]. For BPA degradation, the 1%wt-$FeVO_4/Bi_4O_5Br_2$ photocatalyst exhibited the highest photodegradation

efficiency and k_{app} value (90% and 7.6x10^{-3} min^{-1}, respectively). The k_{app} value for the BPA degradation by 1%wt-$FeVO_4/Bi_4O_5Br_2$ was 2.0 and 19.0 times higher than $Bi_4O_5Br_2$ (7.6x10^{-3} min^{-1}) and $FeVO_4$ (4.0x10^{-4} min^{-1}), respectively (**Figure 7**(d)). This 1%wt-$FeVO_4/Bi_4O_5Br_2$ photocatalyst also exhibited the highest activity among the other $FeVO_4/Bi_4O_5Br_2$ heterojunction photocatalysts. Changes in the UV–vis absorption spectra of the BPA solutions during the photodegradation by 1%wt-$FeVO_4/Bi_4O_5Br_2$ at different irradiation times (0-360 min) are shown in **Figure S3**(b).

For RhB photodegradation (**Figure 7**(b) and (e)), 1%wt-$FeVO_4/Bi_4O_5Br_2$ also exhibited the highest photodegradation efficiency. It was found that 97% of RhB was degraded by 1%wt-$FeVO_4/Bi_4O_5Br_2$ with k_{app} of 3.0×10^{-2} min^{-1}, 84% and 4% of RhB were degraded by $Bi_4O_5Br_2$ and $FeVO_4$ with k_{app} of 2.6×10^{-2} and 4.0×10^{-4} min^{-1}, respectively. Notably, λ_{max} of the degraded RhB solution (**Figure S3**(c)) showed a blue-shift in the absorption spectra from 554 to 496 nm, together with a decrease in absorption intensity, implying that the decomposition of RhB could occur through the stepwise *N*-de-ethylation process [25].

For TC photodegradation (**Figure 7**(c) and (f)), 1%wt-$FeVO_4/Bi_4O_5Br_2$ also exhibited a higher photodegradation efficiency and k_{app} value (88%, 1.7x10^{-2} min^{-1}) than $Bi_4O_5Br_2$ (73%, 1.1x10^{-2} min^{-1}) and $FeVO_4$ (5%, 8.0x10^{-4} min^{-1}). The k_{app} value for the TC photodegradation by 1%wt-$FeVO_4/Bi_4O_5Br_2$ were 1.6 and 21.3 times faster than that of $Bi_4O_5Br_2$ and $FeVO_4$, respectively. Remarkably, $FeVO_4$ exhibited a lower TC photodegradation efficiency when compared to the photolysis of TC. This is probably because the $FeVO_4$ particles were highly suspended throughout the reaction solution, resulting in an increase in the opacity of the solution. The suspension of $FeVO_4$ could scatter the incident light, which would then lead to a reduction in the depth of light penetration. Consequently, this would reduce the numbers of reactive species that are responsible for the TC degradation. Change in the UV–vis absorption

spectra of the remaining TC solutions during the photodegradation reaction by 1%wt-$FeVO_4/Bi_4O_5Br_2$ are shown in **Figure S3**(d).

The photodegradation efficiency plots for the reduction of Cr(VI), and the degradation of BPA, RhB and TC, including adsorption under the dark conditions, are provided to further support the photocatalytic activity of the photocatalyst samples (**Figure S4**(a)-(d)). After being stirred in the dark for 30 min, the $Bi_4O_5Br_2$ photocatalyst exhibited a higher degree of adsorption than $FeVO_4$, suggesting that the $Bi_4O_5Br_2$ microspheres with the porous structure provided a higher surface area than the $FeVO_4$ nanoparticles. Additionally, the 1%wt-$FeVO_4/Bi_4O_5Br_2$ photocatalyst exhibited a higher degree of adsorption than the two single-components. The heterogeneous photocatalytic reactions are known to be surface-related processes. A photocatalyst with a large surface area usually have more active sites, thus providing a positive effect on the catalytic reactions.

Moreover, the N_2 adsorption-desorption isotherms of $FeVO_4$, $Bi_4O_5Br_2$ and 1%wt-$FeVO_4/Bi_4O_5Br_2$ were recorded to elucidate the adsorption ability of the photocatalysts and support the photocatalytic removal results (**Figure S4**(e)). Isotherms of the $Bi_4O_5Br_2$ and 1%wt-$FeVO_4/Bi_4O_5Br_2$ samples were identified as type IV with H3 hysteresis loops, verifying their mesoporous and slit-like pore shapes. However, $FeVO_4$ almost had no hysteresis loop indicating its non-porous structure. The specific surface area of $FeVO_4$, $Bi_4O_5Br_2$ and 1%wt-$FeVO_4/Bi_4O_5Br_2$ were 19.8, 47.0, and 67.1 $m^2\ g^{-1}$, respectively. Compared with $Bi_4O_5Br_2$ and $FeVO_4$, the greater specific surface area of 1%wt-$FeVO_4/Bi_4O_5Br_2$ provided abundant active reaction sites and enabled the adsorption of more pollutant molecules on the photocatalytic surface, which was determined to be beneficial for the enhancement of photocatalytic activity. Notably, the total pore volume of 1%wt-$FeVO_4/Bi_4O_5Br_2$ (0.3680 $cm^3\ g^{-1}$) was slightly smaller than that of $Bi_4O_5Br_2$ (0.3930 $cm^3\ g^{-1}$) suggesting that the porous structure of $Bi_4O_5Br_2$ enabled $FeVO_4$ nanoparticles to be anchored on its surface. The tight coupling between $FeVO_4$ and

$Bi_4O_5Br_2$ in 1%wt-$FeVO_4$/$Bi_4O_5Br_2$ allowed for intimate contact between the surfaces of $Bi_4O_5Br_2$ and $FeVO_4$. This facilitated the charge transfer efficiency at the surface of the 1%wt-$FeVO_4$/$Bi_4O_5Br_2$ nanocomposite during the photocatalytic reactions.

Mineralization is an important target in the complete removal of organic pollutants from wastewater. Thus, TOC analysis was further performed in order to determine the mineralization of BPA, RhB, and TC during the photodegradation process. **Figure S5** shows that, when $Bi_4O_5Br_2$ was used as photocatalyst, 20%, 24%, and 40% of TOC were removed after photodegradation reactions for 360, 120, and 150 min of the BPA, RhB, and TC pollutants. Using 1%wt-$FeVO_4$/$Bi_4O_5Br_2$, TOC decreased by 41%, 43%, and 45% for BPA, RhB and TC after photodegradation reactions for 360, 120, and 150 min, respectively. These results imply that the original organic molecules were partly degraded into CO_2, water, and/or inorganic species. Although the 1%wt-$FeVO_4$/$Bi_4O_5Br_2$ photocatalyst could not achieve complete mineralization, this photocatalyst exhibited a relatively enhanced photocatalytic activity and mineralization ability for these organic molecules in comparison to the $Bi_4O_5Br_2$ photocatalyst. This would be suggestive of its promising efficacy in photocatalytic pollutant degradation.

Based on the photocatalytic activity tests, it can be concluded that 1%wt of $FeVO_4$ was the optimum content in the $FeVO_4$/$Bi_4O_5Br_2$ nanocomposite. Thus, the photocatalytic activity could be significantly increased in terms of both reduction and oxidation of the different targeted pollutants. Coupling 3% and 5%wt of $FeVO_4$ to $Bi_4O_5Br_2$ provided lower photocatalytic activity because an excessive amount of $FeVO_4$ particles may cover the active reaction sites on the $Bi_4O_5Br_2$ surface, while the lower $FeVO_4$ content (0.5%wt) may not be enough to fully and efficiently overcome the rapid e^-/h^+ pairs recombination. Furthermore, the physical mixture of 1%wt of $FeVO_4$ and $Bi_4O_5Br_2$ (denoted as P1%wt-$FeVO_4$/$Bi_4O_5Br_2$) also exhibited lower photocatalytic activity than all of the chemically mixed $FeVO_4$/$Bi_4O_5Br_2$ nanocomposites, indicating that a strong chemical interaction between the two materials is

necessary for the enhanced photocatalytic activity, and the enhanced activity of the nanocomposite originated from the charge transfer at the chemical contact interface between $FeVO_4$ and $Bi_4O_5Br_2$ rather than the simple physical mixture.

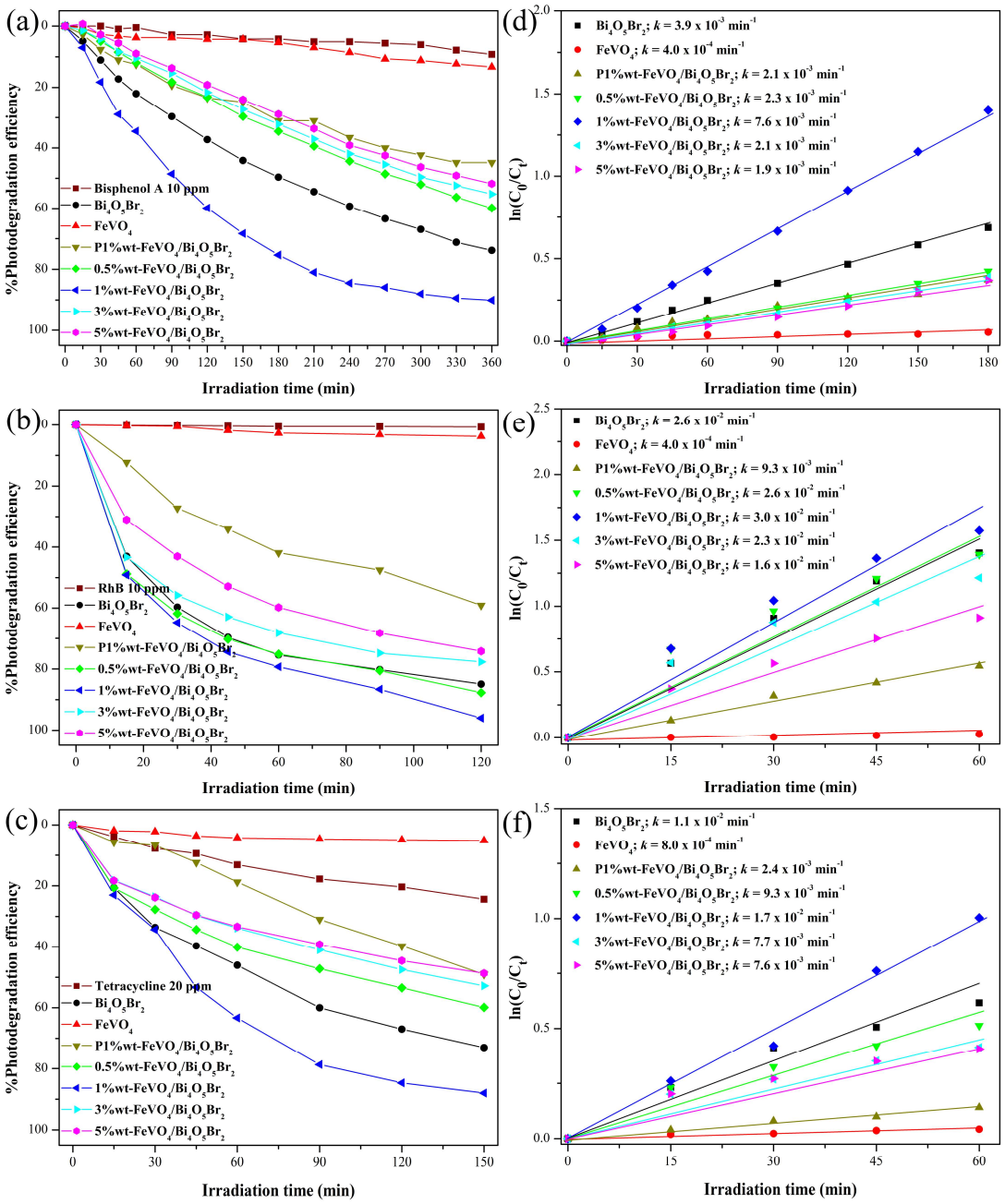

Figure 7. Photodegradation efficiency of (a) BPA, (b) RhB and (c) TC, and kinetic plots of photodegradation of (d) BPA, (e) RhB and (f) TC over $Bi_4O_5Br_2$, $FeVO_4$ and $FeVO_4/Bi_4O_5Br_2$.

To determine the recyclability of the photocatalysts, 1%wt-$FeVO_4/Bi_4O_5Br_2$ was used for photocatalytic removal of Cr(VI), BPA and RhB in four successive runs in comparison to the $Bi_4O_5Br_2$ host material. As is presented in **Figure 8**(a-c), the photocatalytic performances of both $Bi_4O_5Br_2$ and 1%wt-$FeVO_4/Bi_4O_5Br_2$ slightly decreased after four cycles. This result may have been due to the reduced adsorption sites of the photocatalysts that were governed by organic molecules or Cr(VI) ions during the recycling processes. It may have also been due to certain losses in the photocatalyst samples after each cycle. However, 1%wt-$FeVO_4/Bi_4O_5Br_2$ still exhibited a higher photo-efficacy than $Bi_4O_5Br_2$. Additionally, XRD patterns (**Figure 8**(d)) and FESEM images (**Figure S6**) of the photocatalysts after the cyclic degradation experiment displayed no change when compared to the fresh photocatalyst, indicating its long-term stability against photo-corrosion and the applied conditions. The results suggest that the feasibility have been established in applying the 1%wt-$FeVO_4/Bi_4O_5Br_2$ heterojunction for aquatic environmental protection.

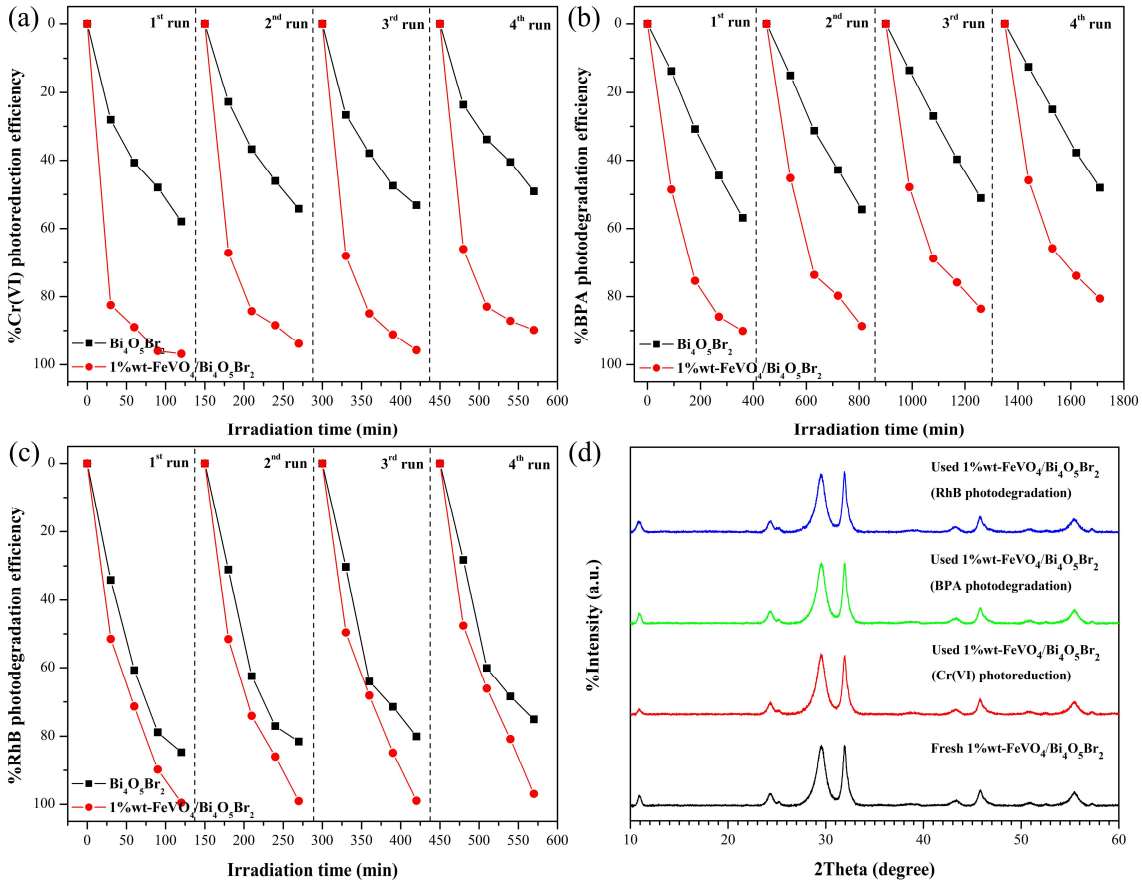

Figure 8. Cycling test for (a) photoreduction of Cr(VI) and photodegradation (b) BPA and (c) RhB over 1%wt-$FeVO_4/Bi_4O_5Br_2$ in comparison with $Bi_4O_5Br_2$. (d) XRD patterns of the fresh and used 1%wt-$FeVO_4/Bi_4O_5Br_2$ photocatalysts.

To identify the active species during photocatalysis, trapping experiments were carried out in the 1%wt-$FeVO_4/Bi_4O_5Br_2$ reaction system. Isopropyl alcohol (IPA), benzoquinone (BQ) or ascorbic acid (ASC), and ammonium oxalate (AO) with 1 mmol L^{-1} were added to the reaction solutions to scavenge hydroxyl radicals (•OH), superoxide radicals ($•O_2^-$), and holes (h^+), respectively [45–47]. The addition of BQ and AO critically suppressed the BPA photodegradation efficiency (**Figure 9**(a)). Similarly, the RhB photodegradation was thoroughly suppressed when ASC and AO were added to the solution (**Figure 9**(b)), indicating that $•O_2^-$ and h^+ were the main active species responsible for the BPA and RhB

photodegradation. However, when using IPA, the photodegradation of both BPA and RhB was slightly decreased, suggesting that •OH plays a minor role in the photodegradation [48].

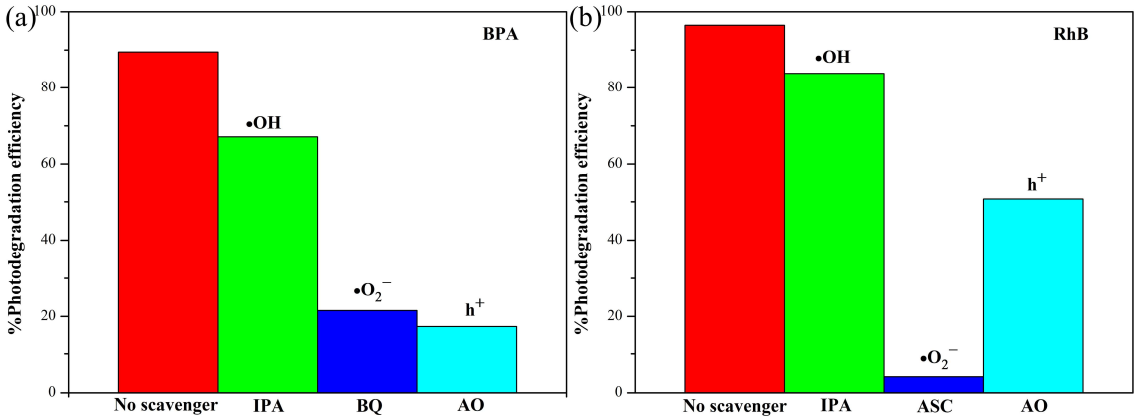

Figure 9. Effect of different scavengers on (a) BPA and (b) RhB photodegradation over 1%wt-$FeVO_4/Bi_4O_5Br_2$.

The nitrotetrazolium blue (NBT) transformation method [49] was used to verify the detection of the generated $•O_2^-$ radicals based on the fact that NBT readily reacts with $•O_2^-$ radicals to form a formazan derivative in an aqueous solution. The NBT solution with the 1%wt-$FeVO_4/Bi_4O_5Br_2$ photocatalyst (or the $Bi_4O_5Br_2$ photocatalyst) was irradiated under 50 W of LED for 360 min, and the NBT supernatant solutions were sampled every 60 min. The absorption intensity of the NBT supernatant solutions at λ_{max} of 265 nm was recorded on the UV-vis spectrophotometer. The absorption spectra of the NBT supernatant solutions after 360 min of irradiation shown in **Figure 10(a)** indicates that the 1%wt-$FeVO_4/Bi_4O_5Br_2$ photocatalyst exhibited a lower intensity of the absorption peak when compared to the $Bi_4O_5Br_2$ photocatalyst. This result implies that the 1%wt-$FeVO_4/Bi_4O_5Br_2$ heterojunction photocatalyst is more efficient in the generation of $•O_2^-$ radicals than the single $Bi_4O_5Br_2$ photocatalyst. The transformation percentages of NBT catalyzed by the photocatalyst samples at every 60 min were then calculated from a decrease in the NBT absorption intensity, and the results are shown

in **Figure 10(b)**. The 1%wt-$FeVO_4/Bi_4O_5Br_2$ photocatalyst provided a higher NBT transformation percentage (90.59%) than the $Bi_4O_5Br_2$ photocatalyst (61.06%), where the yields of generated $\bullet O_2^-$ radicals were calculated to be 36.43 and 27.17 μmol L^{-1} for 1%wt-$FeVO_4/Bi_4O_5Br_2$ and $Bi_4O_5Br_2$, respectively. These results indicate that the efficient separation of electrons and holes derived from the 1%wt-$FeVO_4/Bi_4O_5Br_2$ heterostructure caused the generation of active $\bullet O_2^-$ radicals resulting in enhanced photocatalytic activity.

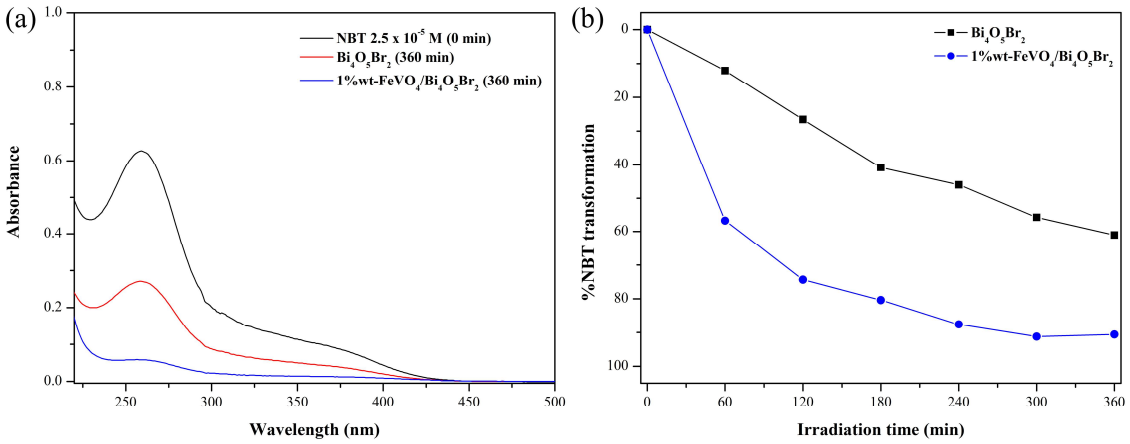

Figure 10. (a) Absorption spectra of the nitrotetrazolium blue solutions catalyzed by 1%wt-$FeVO_4/Bi_4O_5Br_2$ and $Bi_4O_5Br_2$ and (b) NBT transformation percentages after 360 min of visible light irradiation.

The detection of •OH radicals was also confirmed by the terephthalic acid photoluminescence (TA-PL) probing technique [50]. Briefly, terephthalic acid (TA) in a NaOH solution with the 1%wt-$FeVO_4/Bi_4O_5Br_2$ photocatalyst was irradiated under 50 W of LED for 360 min. The terephthalic acid can react with the generated •OH radicals to produce fluorescent 2-hydroxyterephthalic acid (TAOH), which emits photoluminescence at 425 nm on the excitation of 315 nm. The PL intensity of the TAOH solution is proportional to the amount of generated •OH radicals. As is illustrated in **Figure 11**(a), the emission peaks of TAOH exhibited very weak intensity indicating that low amounts of •OH radicals were generated by

the 1%wt-$FeVO_4/Bi_4O_5Br_2$ photocatalyst. Notably, at the initial reactions (120-240 min), the peak intensity was slightly increased, whereas the peak intensity was significantly increased after 240 min of the reaction. It is known that the power for photogenerated electrons to generate •OH radicals is much weaker than that of photogenerated holes [51]. Therefore, it can be suggested that the generated •OH radicals probably occurred from H_2O_2 that was converted from the $•O_2^-$ radicals rather than from the photogenerated holes. These results support the result obtained from the trapping experiment, which indicated that •OH played a minor role in the oxidative degradation of the organic molecules. The detection of H_2O_2 was also confirmed by the *o*-tolidine spectrophotometric method using a solution of 1% *o*-tolidine in 0.1 mol L^{-1} HCl as a peroxide indicator [52,53]. The H_2O_2 specie in the reaction can react with the *o*-tolidine in the HCl solution to produce the protonated form of the 2-electron oxidation product of *o*-tolidine. The UV-vis absorption spectrum of the 2-electron oxidized *o*-tolidine exhibited a characteristic absorption at λ_{max} of 438 nm. **Figure 11**(b) shows that H_2O_2 was generated during the photocatalytic reaction, which could then consequently reduce to the •OH radicals. It should be noted that the absorption intensity the 2-electron oxidized tolidine was much low, thereby H_2O_2 could not be considered significant for the photocatalytic degradation.

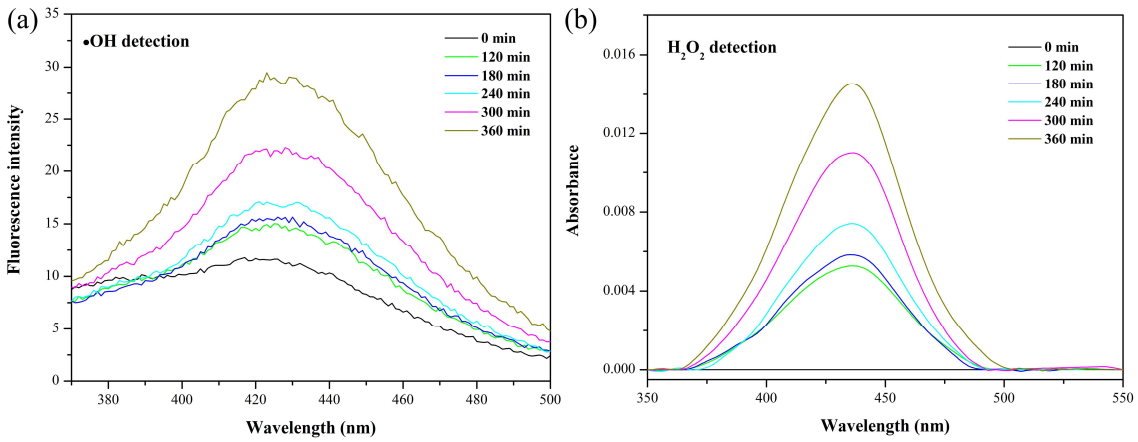

Figure 11. (a) Fluorescence spectra of a 2-hydroxyterephthalic acid solution and (b) UV-vis absorption spectra of the 2-electron oxidized tolidine that was generated by the 1%wt-$FeVO_4/Bi_4O_5Br_2$ photocatalyst under visible light irradiation.

3.5. Charge transfer mechanism

According to the calculated band positions, E_{VB} of $Bi_4O_5Br_2$ (2.41 V *vs.* NHE) is more positive than E_{VB} of $FeVO_4$ (1.43 V *vs.* NHE), while E_{CB} of $FeVO_4$ (-0.63 V *vs.* NHE) is more negative than E_{CB} of $Bi_4O_5Br_2$ (-0.15 V *vs.* NHE), forming the staggered band $FeVO_4/Bi_4O_5Br_2$ structure. In accordance with this band structure, two possible charge transfer pathways have been postulated; conventional type-II and step-scheme (S-scheme) mechanisms. For the conventional type-II mechanism (**Figure 12**(a)), when 1%wt-$FeVO_4/Bi_4O_5Br_2$ heterojunction was excited by visible-light radiation, both components in the heterojunction produced electrons and holes. Simultaneously, the photoexcited electrons (e^-) from the CB of $FeVO_4$ migrated to the CB of $Bi_4O_5Br_2$, meanwhile holes (h^+) from the VB of $Bi_4O_5Br_2$ migrated to the VB of $FeVO_4$. Subsequently, the accumulated electrons in the CB of $Bi_4O_5Br_2$ and the holes in the VB of $FeVO_4$ acted as initiators in the generation of the reactive oxygen species in the photodegradation process. The electrons in the CB of $Bi_4O_5Br_2$ would reduce dissolved O_2 to $\bullet O_2^-$ radicals due to the lower reduction potential (E^0) of $O_2/\bullet O_2^-$ (-0.046 V vs. NHE). However, this reduction was unlikely to have occurred as a consequence of the small potential difference between E_{CB} of $Bi_4O_5Br_2$ and E^0 of $O_2/\bullet O_2^-$, whereby $\bullet O_2^-$ should be considered as a minor active species in the photodegradation process. In addition, holes in the VB of $FeVO_4$ were unable to oxidize OH^- to •OH radicals because the VB of $FeVO_4$ was less positive than E^0 of $OH^-/\bullet OH$ (2.40 V *vs*. NHE). These findings are inconsistent with the results from the trapping experiments and NBT transformation. Therefore, the charge transfer mechanism in the

$FeVO_4/Bi_4O_5Br_2$ heterojunction occurred through the S-scheme mechanism rather than the conventional type-II mechanism.

The S-scheme heterojunction photocatalyst is mainly composed of two n-type semiconductors, including oxidation-type and reduction-type semiconductors. The oxidation-type semiconductor has lower Fermi level, and lower CB and VB positions. On the contrary, the reduction-type semiconductor has higher Fermi level, and higher CB and VB positions [54]. Based on this concept, when n-type $Bi_4O_5Br_2$ and n-type $FeVO_4$ semiconductors were in a close contact to form the $FeVO_4/Bi_4O_5Br_2$ heterojunction (**Figure 12**(b)), the difference in their Fermi level difference as well as CB and VB positions could drive the electron migration at the their interfaces to achieve the Fermi level equilibrium [30,32,55]. As a result, the internal electric field was created at the $FeVO_4/Bi_4O_5Br_2$ interface [33,56]. Under light irradiation, the e^-/h^+ pairs were generated in $FeVO_4$ and $Bi_4O_5Br_2$. Simultaneously, the electrons with relative weak reducibility in the CB of $Bi_4O_5Br_2$ recombined with the weak oxidative holes in the VB of $FeVO_4$ owing to the presence of internal electric field, band edge bending, and Coulomb interaction [57–60]. As a result, the photogenerated electrons reserved in the CB of $FeVO_4$, with a strong reducibility, was sufficient to reduce O_2 to $\bullet O_2^-$ due to its more negative CB potential than E^0 of $O_2/\bullet O_2^-$. Subsequently, the generated $\bullet O_2^-$, together with holes in the VB of $Bi_4O_5Br_2$, reacted with the organic molecules in the photodegradation process. Additionally, some $\bullet O_2^-$ radicals could also be converted to H_2O_2, and then •OH radicals were generated from H_2O_2 as has been previously discussed.

Furthermore, the proposed mechanism for the Cr(VI) photoreduction by 1%wt-$FeVO_4/Bi_4O_5Br_2$ is shown in **Figure 12**(c). The powerful electrons in the CB of $FeVO_4$ reduced Cr(VI) to Cr(III) due to the more positive reduction potentials of $HCrO_4^-/Cr^{3+}$ (1.35 V *vs.* NHE) and $Cr_2O_7^{2-}/Cr^{3+}$ (1.33 V *vs.* NHE) than E_{CB} of $FeVO_4$. At the same time, holes in

the VB of $Bi_4O_5Br_2$ oxidize H_2O to yield O_2 due to the less positive reduction potential of O_2/H_2O (1.23 V *vs.* NHE) than E_{VB} of $Bi_4O_5Br_2$.

In order to further prove the S-scheme charge transfer process, the Ag and PbO_2 photo-deposition experiments were also carried out based on the fact that Ag^+ ion in $AgNO_3$ solution can be reduced to Ag metal by accepting an electron, while Pb^{2+} ions in $Pb(NO_3)_2$ solution can be oxidized to PbO_2 by accepting holes. HRTEM images of the 1%wt-$FeVO_4/Bi_4O_5Br_2$ nanocomposite after being photo-deposited by Ag and PbO_2 are shown in **Figure 13**(a) and (b), respectively. The HRTEM images indicate that the Ag nanoparticle with a lattice fringe of 0.330 nm, which corresponded to the $(0\bar{1}2)$ plane of Ag, was deposited on the surface of $FeVO_4$ (**Figure 13**(a)). Moreover, PbO_2 with a lattice spacing of 0.275 nm, which corresponded to (101) plane of PbO_2, was deposited on the surface of $Bi_4O_5Br_2$ (**Figure 13**(b)) in the 1%wt-$FeVO_4/Bi_4O_5Br_2$ nanocomposite. These results indicate that photo-generated electrons accumulated on the surface of $FeVO_4$, while holes accumulated on the surface of $Bi_4O_5Br_2$. By combining the results from the XPS analysis, Mott-Schottky plots, trapping experiments, NBT transformation and TA-PL experiments, along with the outcomes of the photo-deposition experiments, it is reasonable to conclude that the charge transfer pathway in this $FeVO_4/Bi_4O_5Br_2$ heterojunction followed the S-scheme mechanism.

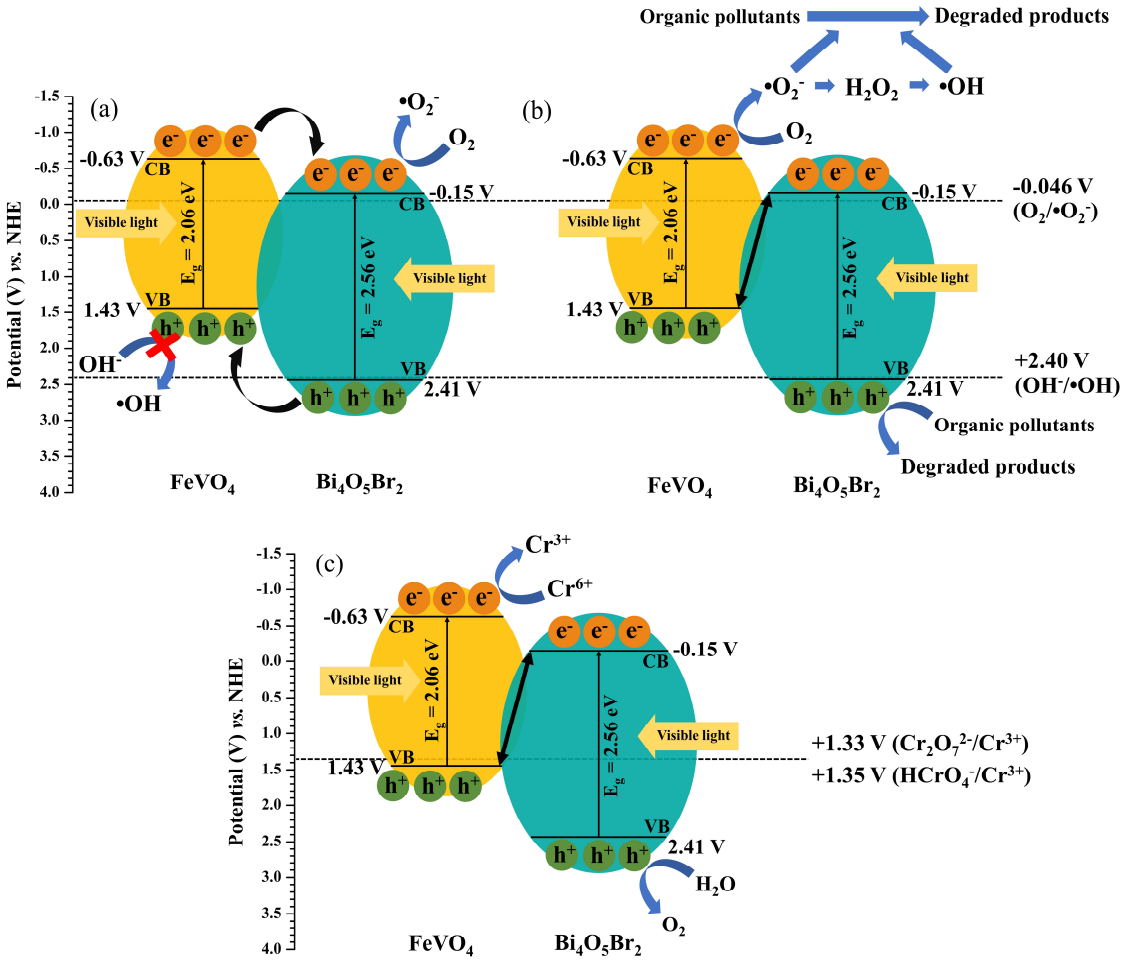

Figure 12. Possible charge transfer and photocatalytic mechanisms for the organic pollutants photodegradation by the 1%wt-$FeVO_4$/$Bi_4O_5Br_2$ heterojunction; (a) conventional type-II and (b) S-scheme mechanisms. (c) Proposed photocatalytic mechanism for the Cr(VI) photoreduction.

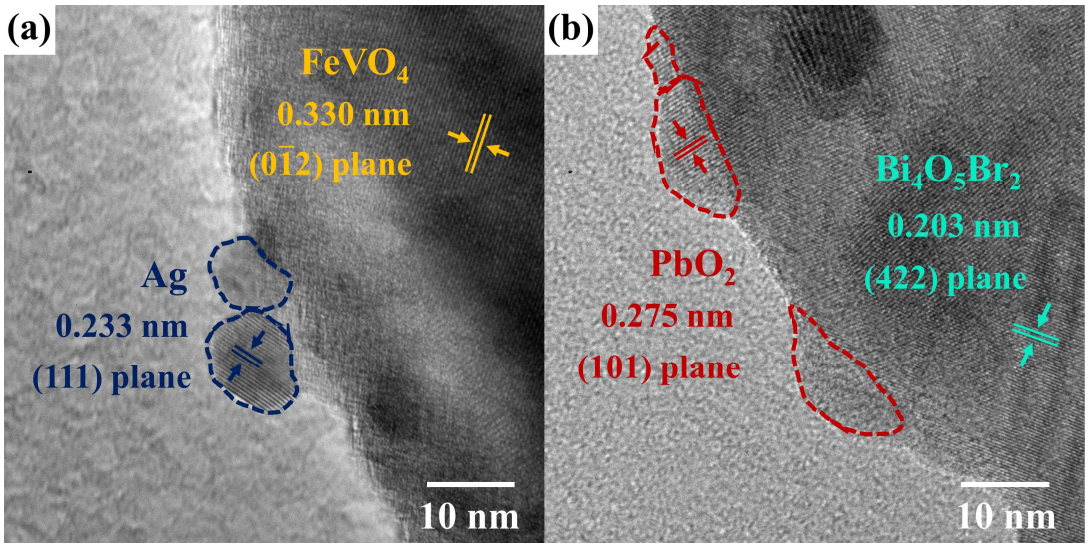

Figure 13. HRTEM images of (a) Ag nanoparticle deposited on the surface of the $FeVO_4$ particle and (b) PbO_2 nanoparticle deposited on the surface of the $Bi_4O_5Br_2$ particle in the 1%wt-$FeVO_4$/$Bi_4O_5Br_2$ nanocomposite.

4. Conclusion

The S-scheme $FeVO_4$/$Bi_4O_5Br_2$ heterojunctions were successfully fabricated by the microwave irradiation combined with wet impregnation methods. Herein, bismuth oxobromides with tuneable chemical composition and morphology were synthesized by microwave irradiation using different kinds of solvents. The 1%wt-$FeVO_4$/$Bi_4O_5Br_2$ heterojunction presented the highest photoreduction of Cr(VI), and degradation of BPA, RhB and TC under visible-light irradiation. Chemical interactions in the $FeVO_4$/$Bi_4O_5Br_2$ nanocomposite facilitated the charge transfer at the heterointerfaces, which resulted in enhanced photocatalytic activity. Recycling experiments demonstrated the excellent recyclability and stability of the heterojunction photocatalyst after four successive photocatalytic reactions for both Cr(VI) photoreduction, and organic molecules degradation. Remarkably, this finding has provided some important guidance for the synthesis and

development of visible-light driven photocatalysts in conjunction with S-scheme photocatalytic systems for environmental rectification under visible-light irradiation.

Acknowledgements

This research project was supported by Thailand Science Research and Innovation (TSRI); and the Program Management Unit for Human Resources & Institutional Development, Research and Innovation, Office of National Higher Education Science Research and Innovation Policy Council (NXPO) [Grant Number B16F640001]. This work was also partially supported by Chiang Mai University, Thailand. We also thanks Science and Technology Service Center, Faculty of Science, Maejo University for SEM and EDS instruments. Tawanwit Luangwanta would like to thank the Development and Promotion of Science and Technology Talents Project (DPST).

Credit authorship contribution statement

Tawanwit Luangwanta: Methodology; Formal analysis; Investigation; Writing - Original draft; Visualization. **Auttaphon Chachvalvutikul:** Methodology; Formal analysis; Investigation. **Sulawan Kaowphong:** Conceptualization; Methodology; Validation; Investigation; Resources; Writing - review & editing; Visualization; Supervision; Project administration; Funding acquisition.

Conflicts of Interests

The authors declare that there are no conflicts of interest.

References

[1] Y.M. Hunge, A.A. Yadav, Basics and advanced developments in photocatalysis – a

review (Mini review), Int. J. Hydrol. 2 (2018) 539–540. https://doi.org/10.15406/ijh.2018.02.00122.

[2] K. Kabra, R. Chaudhary, R.L. Sawhney, Treatment of hazardous organic and inorganic compounds through aqueous-phase photocatalysis: A review, Ind. Eng. Chem. Res. 43 (2004) 7683–7696. https://doi.org/10.1021/ie0498551.

[3] C. Wilson-Frank, Biomarkers in Toxicology, Second ed., Chapter 65 - Proteomics in Biomarkers of Chemical Toxicity, Elsevier Inc., 2019, pp. 1153-1163. https://doi.org/10.1016/b978-0-12-814655-2.00065-7.

[4] J.B. Islam, M. Furukawa, I. Tateishi, H. Katsumata, S. Kaneco, Photocatalytic reduction of hexavalent chromium with nanosized TiO_2 in presence of formic acid, ChemEngineering. 3 (2019) 1–10. https://doi.org/10.3390/chemengineering3020033.

[5] F.E.B. Coelho, V.M. Candelario, E.M.R. Araújo, T.L.S. Miranda, G. Magnacca, Photocatalytic reduction of Cr(VI) in the presence of humic acid using immobilized ce–Zro2 under visible light, Nanomaterials. 10 (2020). https://doi.org/10.3390/nano10040779.

[6] A. Careghini, A.F. Mastorgio, S. Saponaro, E. Sezenna, Bisphenol A, nonylphenols, benzophenones, and benzotriazoles in soils, groundwater, surface water, sediments, and food: a review, Environ. Sci. Pollut. Res. 22 (2015) 5711–5741. https://doi.org/10.1007/s11356-014-3974-5.

[7] R. Jain, M. Mathur, S. Sikarwar, A. Mittal, Removal of the hazardous dye rhodamine B through photocatalytic and adsorption treatments, J. Environ. Manage. 85 (2007) 956–964. https://doi.org/10.1016/j.jenvman.2006.11.002.

[8] A.A. Borghi, M.S.A. Palma, Tetracycline: Production, waste treatment and environmental impact assessment, Brazilian J. Pharm. Sci. 50 (2014) 25–40. https://doi.org/10.1590/S1984-82502011000100003.

[9] J. You, Y. Guo, R. Guo, X. Liu, A review of visible light-active photocatalysts for water disinfection: Features and prospects, Chem. Eng. J. 373 (2019) 624–641. https://doi.org/10.1016/j.cej.2019.05.071.

[10] J. Li, Y. Yu, L. Zhang, Bismuth oxyhalide nanomaterials: Layered structures meet photocatalysis, Nanoscale. 6 (2014) 8473–8488. https://doi.org/10.1039/c4nr02553a.

[11] G. Zhu, M. Hojamberdiev, W. Zhang, S. Taj Ud Din, Y. Joong Kim, J. Lee, W. Yang, Enhanced photocatalytic activity of Fe-doped $Bi_4O_5Br_2$ nanosheets decorated with Au nanoparticles for pollutants removal, Appl. Surf. Sci. 526 (2020) 146760. https://doi.org/10.1016/j.apsusc.2020.146760.

[12] J. Shang, W. Hao, X. Lv, T. Wang, X. Wang, Y. Du, S. Dou, T. Xie, D. Wang, J. Wang, Bismuth oxybromide with reasonable photocatalytic reduction activity under visible light, ACS Catal. 4 (2014) 954–961. https://doi.org/10.1021/cs401025u.

[13] R. Li, F. Xie, J. Liu, Y. Wang, Y. Wang, X. Zhang, C. Fan, Synthesis of $Bi_4O_5Br_2$ from reorganization of BiOBr and its excellent visible light photocatalytic activity, Dalt. Trans. 45 (2016) 9182–9186. https://doi.org/10.1039/c6dt00997b.

[14] K. Sridharan, S. Shenoy, S.G. Kumar, C. Terashima, A. Fujishima, S. Pitchaimuthu, Advanced two-dimensional heterojunction photocatalysts of stoichiometric and non-stoichiometric bismuth oxyhalides with graphitic carbon nitride for sustainable energy and environmental applications, Catalysts. 11 (2021) 426. https://doi.org/10.3390/catal11040426.

[15] J. Xia, Y. Ge, J. Di, L. Xu, S. Yin, Z. Chen, P. Liu, H. Li, Ionic liquid-assisted strategy for bismuth-rich bismuth oxybromides nanosheets with superior visible light-driven photocatalytic removal of bisphenol-A, J. Colloid Interface Sci. 473 (2016) 112–119. https://doi.org/10.1016/j.jcis.2016.03.046.

[16] L. Ye, X. Jin, C. Liu, C. Ding, H. Xie, K.H. Chu, P.K. Wong, Thickness-ultrathin and

bismuth-rich strategies for BiOBr to enhance photoreduction of CO_2 into solar fuels, Appl. Catal. B Environ. 187 (2016) 281–290. https://doi.org/10.1016/j.apcatb.2016.01.044.

[17] J. Liu, R. Li, X. Zu, X. Zhang, Y. Wang, Y. Wang, C. Fan, Photocatalytic conversion of nitrogen to ammonia with water on triphase interfaces of hydrophilic-hydrophobic composite $Bi_4O_5Br_2$/ZIF-8, Chem. Eng. J. 371 (2019) 796–803. https://doi.org/10.1016/j.cej.2019.03.283.

[18] J. Xu, Y.G. Mao, T. Liu, Y. Peng, Synthesis of a novel one-dimensional BiOBr-$Bi_4O_5Br_2$ heterostructure with a high quality interface and its enhanced visible-light photocatalytic activity, CrystEngComm. 20 (2018) 2292–2298. https://doi.org/10.1039/c8ce00157j.

[19] R. Marschall, Semiconductor composites: Strategies for enhancing charge carrier separation to improve photocatalytic activity, Adv. Funct. Mater. 24 (2014) 2421–2440. https://doi.org/10.1002/adfm.201303214.

[20] S.J. Hu, J. Yang, X.H. Liao, Highly efficient degradation of methylene blue on microwave synthesized $FeVO_4$ nanoparticles photocatalysts under visible-light irradiation, Appl. Mech. Mater. 372 (2013) 153–157. https://doi.org/10.4028/www.scientific.net/AMM.372.153.

[21] B. Ozturk, G.S. Pozan Soylu, Synthesis of surfactant-assisted $FeVO_4$ nanostructure: Characterization and photocatalytic degradation of phenol, J. Mol. Catal. A Chem. 398 (2015) 65–71. https://doi.org/10.1016/j.molcata.2014.11.013.

[22] M.M. Sajid, S.B. Khan, N.A. Shad, N. Amin, Z. Zhang, Visible light assisted photocatalytic degradation of crystal violet dye and electrochemical detection of ascorbic acid using a $BiVO_4$/$FeVO_4$ heterojunction composite, RSC Adv. 8 (2018) 23489–23498. https://doi.org/10.1039/c8ra03890b.

[23] X. Liu, Y. Kang, Synthesis and high visible-light activity of novel $Bi_2O_3/FeVO_4$ heterojunction photocatalyst, Mater. Lett. 164 (2016) 229–231. https://doi.org/10.1016/j.matlet.2015.10.137.

[24] A. Chachvalvutikul, J. Jakmunee, S. Thongtem, S. Kittiwachana, S. Kaowphong, Novel $FeVO_4/Bi_7O_9I_3$ nanocomposite with enhanced photocatalytic dye degradation and photoelectrochemical properties, Appl. Surf. Sci. 475 (2019) 175–184. https://doi.org/10.1016/j.apsusc.2018.12.214.

[25] A. Chachvalvutikul, S. Kaowphong, Direct Z-scheme $FeVO_4$/BiOCl heterojunction as a highly efficient visible-light-driven photocatalyst for photocatalytic dye degradation and Cr(VI) reduction, Nanotechnology. 31 (2020) 145704. https://doi.org/10.1088/1361-6528/ab61d1.

[26] Y.-J. Zhu, F. Chen, Microwave-assisted preparation of inorganic nanostructures in liquid phase, Chem. Rev. 114 (2013) 6462–6555. https://doi.org/10.1021/cr400366s.

[27] J. Hu, S. Weng, Z. Zheng, Z. Pei, M. Huang, P. Liu, Solvents mediated-synthesis of BiOI photocatalysts with tunable morphologies and their visible-light driven photocatalytic performances in removing of arsenic from water, J. Hazard. Mater. 264 (2014) 293–302. https://doi.org/10.1016/j.jhazmat.2013.11.027.

[28] Q.C. Liu, D.K. Ma, Y.Y. Hu, Y.W. Zeng, S.M. Huang, Various bismuth oxyiodide hierarchical architectures: Alcohothermal-controlled synthesis, photocatalytic activities, and adsorption capabilities for phosphate in water, ACS Appl. Mater. Interfaces. 5 (2013) 11927–11934. https://doi.org/10.1021/am4036702.

[29] Y. Bai, P. Yang, L. Wang, B. Yang, H. Xie, Y. Zhou, L. Ye, Ultrathin $Bi_4O_5Br_2$ nanosheets for selective photocatalytic CO_2 conversion into CO, Chem. Eng. J. 360 (2019) 473–482. https://doi.org/10.1016/j.cej.2018.12.008.

[30] X. Ke, J. Zhang, K. Dai, K. Fan, C. Liang, Integrated S-scheme heterojunction of amine-

functionalized 1D CdSe nanorods anchoring on ultrathin 2D $SnNb_2O_6$ nanosheets for robust solar-driven CO_2 conversion, Sol. RRL. 5 (2021) 2000805. https://doi.org/10.1002/solr.202000805.

[31] X. Li, J. Zhang, Y. Huo, K. Dai, S. Li, S. Chen, Two-dimensional sulfur- and chlorine-codoped g-C_3N_4/CdSe-amine heterostructures nanocomposite with effective interfacial charge transfer and mechanism insight, Appl. Catal. B Environ. 280 (2021) 119452. https://doi.org/10.1016/j.apcatb.2020.119452.

[32] Y. Huo, J. Zhang, K. Dai, C. Liang, Amine-modified S-scheme porous g-C_3N_4/CdSe-diethylenetriamine composite with enhanced photocatalytic CO_2 reduction activity, ACS Appl. Energy Mater. 4 (2021) 956–968. https://doi.org/10.1021/acsaem.0c02896.

[33] Y. Zhen, C. Yang, H. Shen, W. Xue, C. Gu, J. Feng, Y. Zhang, F. Fu, Y. Liang, Photocatalytic performance and mechanism insights of a S-scheme g-C_3N_4/Bi_2MoO_6 heterostructure in phenol degradation and hydrogen evolution reactions under visible light, Phys. Chem. Chem. Phys. 22 (2020) 26278–26288. https://doi.org/10.1039/d0cp02199g.

[34] F. Mei, Z. Li, K. Dai, J. Zhang, C. Liang, Step-scheme porous g-C_3N_4/$Zn_{0.2}Cd_{0.8}S$-DETA composites for efficient and stable photocatalytic H_2 production, Chinese J. Catal. 41 (2020) 41–49. https://doi.org/10.1016/S1872-2067(19)63389-9.

[35] W. Pudkon, S. Kittiwachana, T. Thongtem, S. Thongtem, S. Kaowphong, Influence of mixed solvents on characteristics and photoluminescence of $GdVO_4$: Eu^{3+}nanophosphors synthesized by solvothermal method, Sci. Adv. Mater. 8 (2016) 138-143. https://doi.org/10.1166/sam.2016.2617.

[36] Y. Xie, F. Chang, C. Li, J. Chen, J. Luo, L. Li, X. Hu, One-pot polyvinyl alcohol-assisted hydrothermal synthesis of hierarchical flower-like BiOCl nanoplates with enhancement of photocatalytic activity for degradation of rhodamine B, Clean - Soil, Air, Water. 42

(2014) 521–527. https://doi.org/10.1002/clen.201300014.

[37] J.T.S. Irvine, D.C. Sinclair, A.R. West, Electroceramics: Characterization by impedance spectroscopy, Adv. Mater. 2 (1990) 132–138. https://doi.org/10.1002/adma.19900020304.

[38] S. Sun, W. Wang, L. Zhang, Bi_2WO_6 quantum dots decorated reduced graphene oxide: Improved charge separation and enhanced photoconversion efficiency, J. Phys. Chem. C. 117 (2013) 9113–9120. https://doi.org/10.1021/jp4004592.

[39] J.W. Zhang, G. Cao, H.Y. Wang, P.Z. Feng, Z.S. Liu, Graphene-$Bi_{24}O_{31}Br_{10}$ composites with tunable architectures for enhanced photocatalytic activity and mechanism, Ceram. Int. 42 (2016) 11796–11804. https://doi.org/10.1016/j.ceramint.2016.04.100.

[40] H. Huang, X. Li, X. Han, N. Tian, Y. Zhang, T. Zhang, Moderate band-gap-broadening induced high separation of electron-hole pairs in Br substituted BiOI: A combined experimental and theoretical investigation, Phys. Chem. Chem. Phys. 17 (2015) 3673–3679. https://doi.org/10.1039/c4cp04842c.

[41] G. Zhu, S. Li, J. Gao, F. Zhang, C. Liu, Q. Wang, M. Hojamberdiev, Constructing a 2D/2D $Bi_2O_2CO_3/Bi_4O_5Br_2$ heterostructure as a direct Z-scheme photocatalyst with enhanced photocatalytic activity for NOx removal, Appl. Surf. Sci. 493 (2019) 913–925. https://doi.org/10.1016/j.apsusc.2019.07.119.

[42] H. Dong, S. Hong, P. Zhang, S. Yu, Y. Wang, S. Yuan, H. Li, J. Sun, G. Chen, C. Li, Metal-free Z-scheme 2D/2D VdW heterojunction for high-efficiency and durable photocatalytic H_2 production, Chem. Eng. J. 395 (2020) 125150. https://doi.org/10.1016/j.cej.2020.125150.

[43] H. Dong, Y. Zuo, N. Song, S. Hong, M. Xiao, D. Zhu, J. Sun, G. Chen, C. Li, Bimetallic synergetic regulating effect on electronic structure in cobalt/vanadium co-doped carbon nitride for boosting photocatalytic performance, Appl. Catal. B Environ. 287 (2021)

119954. https://doi.org/10.1016/j.apcatb.2021.119954.

[44] Y. Chen, C. Hu, J. Qu, M. Yang, Photodegradation of tetracycline and formation of reactive oxygen species in aqueous tetracycline solution under simulated sunlight irradiation, J. Photochem. Photobiol. A Chem. 197 (2008) 81–87. https://doi.org/10.1016/j.jphotochem.2007.12.007.

[45] S. Dong, L. Cui, C. Liu, F. Zhang, K. Li, L. Xia, X. Su, J. Feng, Y. Zhu, J. Sun, Fabrication of 3D ultra-light graphene aerogel/Bi_2WO_6 composite with excellent photocatalytic performance : A promising photocatalysts for water purification, J. Taiwan Inst. Chem. Eng. 97 (2019) 288–296. https://doi.org/10.1016/j.jtice.2019.02.016.

[46] H. Yi, M. Jiang, D. Huang, G. Zeng, C. Lai, L. Qin, C. Zhou, B. Li, X. Liu, M. Cheng, W. Xue, P. Xu, C. Zhang, Advanced photocatalytic Fenton-like process over biomimetic hemin-Bi_2WO_6 with enhanced pH, J. Taiwan Inst. Chem. Eng. 93 (2018) 184–192. https://doi.org/10.1016/j.jtice.2018.06.037.

[47] Q. Zhou, L. Zhang, P. Zuo, Y. Wang, Z. Yu, Enhanced photocatalytic performance of spherical BiOI/MnO_2 composite and mechanism investigation, RSC Adv. 8 (2018) 36161–36166. https://doi.org/10.1039/c8ra06930a.

[48] X. Zhang, P. Yang, B. Yang, Y. Bai, W. Liu, Q. Wang, Synthesis of novel Bi/$Bi_4O_5Br_2$ via a UV light irradiation for decomposing the oil field pollutants, Inorg. Chem. Commun. 122 (2020) 108297. https://doi.org/10.1016/j.inoche.2020.108297.

[49] A. Chachvalvutikul, T. Luangwanta, S. Pattisson, G.J. Hutchings, S. Kaowphong, Enhanced photocatalytic degradation of organic pollutants and hydrogen production by a visible light–responsive Bi_2WO_6/$ZnIn_2S_4$ heterojunction, Appl. Surf. Sci. 544 (2020) 148885. https://doi.org/10.1016/j.apsusc.2020.148885.

[50] D. Majhi, K. Das, A. Mishra, R. Dhiman, B.G. Mishra, One pot synthesis of

CdS/BiOBr/$Bi_2O_2CO_3$: A novel ternary double Z-scheme heterostructure photocatalyst for efficient degradation of atrazine, Appl. Catal. B Environ. 260 (2020) 118222. https://doi.org/10.1016/j.apcatb.2019.118222.

[51] L. Zhang, W. Wang, S. Sun, Y. Sun, E. Gao, Z. Zhang, Elimination of BPA endocrine disruptor by magnetic BiOBr@SiO_2@Fe_3O_4 photocatalyst, Appl. Catal. B Environ. 148–149 (2014) 164–169. https://doi.org/10.1016/j.apcatb.2013.10.053.

[52] L. Wang, S. Cao, K. Guo, Z. Wu, Z. Ma, L. Piao, Simultaneous hydrogen and peroxide production by photocatalytic water splitting, Chinese J. Catal. 40 (2019) 470–475. https://doi.org/10.1016/s1872-2067(19)63274-2.

[53] J. Liu, Y. Zhang, L. Lu, G. Wu, W. Chen, Self-regenerated solar-driven photocatalytic water-splitting by urea derived graphitic carbon nitride with platinum nanoparticles, Chem. Commun. 48 (2012) 8826–8828. https://doi.org/10.1039/c2cc33644h.

[54] Y. Chen, F. Su, H. Xie, R. Wang, C. Ding, J. Huang, Y. Xu, L. Ye, One-step construction of S-scheme heterojunctions of N-doped MoS_2 and S-doped g-C_3N_4 for enhanced photocatalytic hydrogen evolution, Chem. Eng. J. 404 (2021) 126498. https://doi.org/10.1016/j.cej.2020.126498.

[55] Y. Jia, S. Li, J. Gao, G. Zhu, F. Zhang, X. Shi, Y. Huang, C. Liu, Highly efficient $(BiO)_2CO_3$-BiO_{2-x}-graphene photocatalysts: Z-Scheme photocatalytic mechanism for their enhanced photocatalytic removal of NO, Appl. Catal. B Environ. 240 (2019) 241–252. https://doi.org/10.1016/j.apcatb.2018.09.005.

[56] T. Hu, K. Dai, J. Zhang, S. Chen, Noble-metal-free Ni_2P modified step-scheme $SnNb_2O_6$/CdS-diethylenetriamine for photocatalytic hydrogen production under broadband light irradiation, Appl. Catal. B Environ. 269 (2020) 118844. https://doi.org/10.1016/j.apcatb.2020.118844.

[57] Q. Xu, L. Zhang, B. Cheng, J. Fan, J. Yu, S-Scheme heterojunction photocatalyst, Chem.

6 (2020) 1543–1559. https://doi.org/10.1016/j.chempr.2020.06.010.

[58] L. Liu, T. Hu, K. Dai, J. Zhang, C. Liang, A novel step-scheme $BiVO_4/Ag_3VO_4$ photocatalyst for enhanced photocatalytic degradation activity under visible light irradiation, Chinese J. Catal. 42 (2020) 46–55. https://doi.org/10.1016/S1872-2067(20)63560-4.

[59] J. Li, M. li, Z. Jin, Rational design of a cobalt sulfide/bismuth sulfide S-scheme heterojunction for efficient photocatalytic hydrogen evolution, J. Colloid Interface Sci. 592 (2021) 237–248. https://doi.org/10.1016/j.jcis.2021.02.053.

[60] J. Wang, G. Wang, B. Cheng, J. Yu, J. Fan, Sulfur-doped g-C_3N_4/TiO_2 S-scheme heterojunction photocatalyst for Congo Red photodegradation, Chinese J. Catal. 42 (2020) 56–68. https://doi.org/10.1016/S1872-2067(20)63634-8.